

Far-Infrared Spectral Energy Distributions of Embedded Protostars and Dusty Galaxies: I. Theory for Spherical Sources

Sukanya Chakrabarti¹ and Christopher F. McKee^{1,2}

ABSTRACT

We present analytic radiative transfer solutions for the spectra of unresolved, spherically symmetric, centrally heated, dusty sources. We find that the dust thermal spectrum possesses scaling relations that provide a natural classification for a broad range of sources, from low-mass protostars to dusty galaxies. In particular, we find that, given our assumptions, spectral energy distributions (SEDs) can be characterized by two distance-independent parameters, the luminosity-to-mass ratio, L/M , and the surface density, Σ , for a set of two functions, namely, the density profile and the opacity curve. The goal is to use SEDs as a diagnostic tool in inferring the large-scale physical conditions in protostellar and extragalactic sources, and ultimately, evolutionary parameters. Our approach obviates the need to use SED templates in the millimeter to far-infrared region of the spectrum; this is a common practice in the extragalactic community that relies on observed correlations established at low redshift that may not necessarily extend to high redshift. Further, we demarcate the limited region of parameter space in which density profiles can be inferred from the SED, which is of particular import in the protostellar community as competing theories of star formation are characterized by different density profiles. The functionality of our model is unique in that it provides for a self-consistent analytic solution that we have validated by comparison with a well-tested radiative transfer code (DUSTY) to find excellent agreement with numerical results over a parameter space that spans low-mass protostars to ultra-luminous infrared galaxies (ULIRGS).

Subject headings: galaxies: formation—galaxies: starburst—infrared: galaxies—radiative transfer—stars: formation

1. Introduction

Stars and galaxies are born in dusty environments, shielded from view in the optical and often in the near-infrared. Radiation emitted by protostars and newly formed stars is absorbed by dust

¹ Department of Physics, University of California at Berkeley, Mail Code 7300, Berkeley, CA 94720 USA; sukanya@astro.berkeley.edu.

² Department of Astronomy, University of California at Berkeley, Mail Code 3411, Berkeley, CA 94720 USA; cmckee@astro.berkeley.edu.

and re-radiated at infrared and longer wavelengths. One of the primary tools for determining the physical parameters of these sources is the spectral energy distribution, or SED.

The classic example of the use of SEDs to infer the nature of the underlying source is the classification of low-mass protostars based on the slope of their near-mid IR spectra (Lada & Wilking 1984; Lada 1987; Adams, Lada, & Shu 1987): Class I objects, with $d(\nu F_\nu)/d \ln \nu < 0$ in the 2-20 μm region of the spectrum, are identified with protostars; Class II objects, with $0 < d(\nu F_\nu)/d \ln \nu \lesssim 2$, are identified with classical T Tauri stars; and Class III objects, with $2 \lesssim d(\nu F_\nu)/d \ln \nu \leq 3$, are reddened stars approaching the main sequence. Subsequently, a fourth category, Class 0, was added for sources that are so embedded that it is generally not possible to measure the slope of the SED in the near-mid IR (Andre, Ward-Thompson, & Barsony 1993).

The physical interpretation of observations of massive protostars has proven to be a more challenging task. The task of interpretation is complicated by the greater extinction in high-mass star-forming regions and by the fact that massive stars often form in clusters. As a result, there is little consensus on either the evolutionary parameters or the source parameters characteristic of massive star-forming regions. Even such a fundamental parameter as the formation time of a massive star has been uncertain by orders of magnitude. Nakano et al. (2000) interpreted near-IR spectroscopic data of a source in Orion as indicating a formation timescale of the order of 10^3 yr. Osorio, Lizano, & D’Alessio (1999, henceforth OLD99) estimated formation timescales of order 10^4 yr from modeling the SEDs of hot cores. Estimates of formation timescales based on extrapolating the theory of low-mass star formation give formation times greater than 10^6 yr, which is a significant fraction of the lifetime of the main-sequence lifetime of a massive star (McLaughlin & Pudritz 1997, Stahler, Palla, & Ho 2000). Subsequently, McKee & Tan (2002; 2003, henceforth, MT03) developed the Turbulent Core Model for high-mass star formation, which incorporates the effects of the supersonic turbulence and high pressures observed in massive star-forming regions (Plume et al. 1997) and predicts formation timescales of the order of 10^5 yr.

Other basic characteristics of high-mass star-forming regions, also remain uncertain. Only recently has it become possible to observe individual massive star-forming cores (Beuther & Schilke 2004, Cesaroni et al 1999, Fontani et al 2004), yet their properties remain uncertain because of the limited information on the SED. The density profile in high-mass star-forming regions is known only to be in the range of 1 to 2, with significant error bars (Shirley et al 2002, Beuther et al 2002, Jorgensen et al 2002, van der Tak et al 2000, Mueller et al 2002). On the other hand, OLD99 have argued for a more precise value, stating that their data on dust continuum emission from hot cores are best fit by so-called logatropic density profiles, with a power law index of 1. A self-consistent, analytic methodology for the inference of source and evolutionary parameters from the observed far-IR SEDs of protostellar regions would allow us to derive the large scale physical conditions of star-forming regions, and ultimately to discriminate between competing theories of star formation.

A significant fraction of the star formation in the universe comes from dusty galaxies (Genzel & Cesarsky 2000), including ultra-luminous infrared galaxies (ULIRGs), with luminosities between

8 μm and 1 mm in excess of $10^{12}L_{\odot}$ (Soifer et al. 1984), and sub-millimeter galaxies at high redshifts (Smail et al 1997, Barger et al 1999a, Blain et al 2002), which appear to be even more luminous. SEDs are a primary tool for inferring the properties of these sources. The lack of data on high-redshift sources has led to the use of SED templates from low-redshift sources to infer star formation rates in high-redshift sources (e.g., Xu et al 2001, Carilli & Yun 1999, Yun & Carilli 2002, henceforth YC02), but it is not known whether these templates are valid. The discovery of massive, luminous sub-millimeter galaxies may warrant a revision of the star formation history of galaxies at high redshift (Blain et al. 2002) and has been suggested as being problematic for hierarchical formation scenarios (Genzel et al. 2003). The importance of understanding the SEDs of high-redshift galaxies is highlighted by the work of Chapman et al. (2004), who have proposed that higher temperatures in these sources mean that current sub-mm surveys may have missed more than half of the most luminous, dusty galaxies at $z \sim 2$.

The simplest model for an SED is to assume that it is due to an isothermal distribution of optically thin dust (Hildebrand 1983). The next level of sophistication is to allow for the dust to be optically thick above some critical frequency, while still considering the entire dust envelope as being characterized by a single temperature, e.g., Yun & Carilli 2002, henceforth YC02. A difficulty with such single-temperature models is that they often require β to be less than the value appropriate for uncoagulated grain models ($\beta \simeq 2$; Weingartner & Draine 2001). This difficulty can be overcome if the spectrum is assumed to result from the superposition of two blackbodies at different temperatures (Dunne & Eales 2001).

In reality, the dust temperature varies continuously. Variation of the dust temperature has been taken into account in work on low-mass star formation beginning with the pioneering work of Larson (1969), who introduced a physically motivated approximation for the temperature profile. Adams & Shu (1985) presented an approximate numerical radiative transfer model based on this form of the temperature profile and showed that they could approximately satisfy radiative equilibrium. With this model, they inferred stellar masses and accretion rates for their favored collapse model, the singular isothermal sphere. This paper heralded the beginning of a stream of papers on more refined numerical modeling of low-mass protostellar spectra, with inclusion of effects for more evolved sources. Kenyon, Calvet, & Hartmann (1993) developed an approximate numerical approach in which the temperature profile is calculated from the radiative diffusion equation in the optically thick part of the envelope and from radiative equilibrium in the optically thin part. OLD99 adopted this approach in their calculation of the SEDs of massive protostars. Numerical modeling has also enabled the modeling of axisymmetric sources, including disks (Efsthathiou & Rowan-Robinson 1991; Kenyon et al 1993; Whitney et al 2003). However, analytic radiative transfer models for even the simplest spherically symmetric systems remain rare. An exception is that of Adams (1991), who presented an analytic solution for the specific intensity of protostellar cores at millimeter and sub-millimeter wavelengths; however, he did not evaluate the accuracy of his method.

While numerical models permit one to calculate the SED of a given source with exquisite accuracy, what is lacking is any general understanding of how the SED depends on the underlying

source parameters. A significant step in addressing this problem was taken by Ivezić & Elitzur (1997, henceforth IE97), who emphasized the importance of scaling relations in determining the spectrum of dusty sources. They showed that the spectrum of a spherically symmetric, dusty source is determined by four parameters: the dust destruction radius, R_{dd} , which depends on the luminosity of the source (see Appendix A); the thickness of the shell around the source, $y \equiv R_c/R_{\text{dd}}$, where R_c is the radius of the cloud in which the source is embedded; the optical depth through the shell at some frequency; and the temperature of the central source. In addition, the spectrum depends on two functions, the density distribution, $\rho(r)$, and the opacity, κ_ν . Using these scaling properties of dust emission, they developed a numerical code, DUSTY, that is very useful in inferring the physical conditions in dusty sources.

Our objective in this paper is to develop an analytic theory for the SED of spherically symmetric, dusty sources. We assume that the dusty envelope surrounding the central source of radiation is sufficiently opaque that the resultant SED is approximately independent of the temperature of the central source and of the properties of the dust destruction front. Within our parameter space, $100 \text{ g cm}^{-2} \gtrsim \Sigma \gtrsim 0.03 \text{ g cm}^{-2}$, the optical depth is large enough that essentially all the stellar radiation is absorbed by dust and re-emitted. Because of the large optical depth, the near-infrared and optical spectrum, which does depend on the source spectrum, is heavily attenuated. For a given form for the density distribution (e.g., a power-law) and the opacity (e.g., that of Weingartner & Draine 2001), the emergent spectrum depends on three parameters: the luminosity, L ; the dust mass, $M_{\text{dust}} = M/Z_{\text{dust}}$, where Z_{dust} is the mass fraction of dust; and the radius of the source, R_c . The *shape* of the SED is independent of the distance, and therefore depends on only two parameters, which we take to be the luminosity-to-mass ratio, L/M , and the surface density of the source, $\Sigma \equiv M/(\pi R_c^2)$. As we shall show, it is possible to infer these two distance-independent parameters, *and therefore the complete shape of the SED*, from just two colors (provided, of course, that the assumptions underlying our model are correct). Since the pressure in a self-gravitating gas is of order $G\Sigma^2$, determination of the surface density allows one to infer the pressure in the source. If the distance is also known, we can infer the luminosity, dust mass, and physical size of a protostellar region—even if the source is unresolved. However, it is generally not feasible to infer the density profile from the far-IR SED of an unresolved source; as we shall see later, this is feasible for extended envelopes, which are large compared to the radius of the effective photosphere, and for envelopes that emit most of their radiation at wavelengths shorter than $30 \mu\text{m}$.

We find that the spectra are characterized by three frequency regimes: Low frequencies, which are always in the Rayleigh-Jeans limit [$h\nu < kT(R_c)$]; intermediate frequencies, which are not necessarily in the Rayleigh-Jeans limit, but are low enough that the envelope is transparent; and high frequencies, where the spectrum is determined by competition between opacity effects and the Wien cutoff. Having found formal solutions in these three regimes, we present a joint solution within a conceptually simple and physically motivated framework in which the emission in each frequency regime comes from a shell of some thickness, centered at some radius, and is attenuated by the intervening optical depth. We adopt a self-consistent temperature profile that characterizes

the emission coming from the vicinity of an effective Rosseland photosphere. The slope of this profile is set by the condition that the emergent luminosity equal the input luminosity. We have tested the accuracy of our analytic solution by making detailed comparisons with DUSTY.

The organization of the paper is as follows: in §2 we outline the general formulation of the problem, and specify the forms of the density profiles that we consider as well as the dust opacity. In §3 we introduce the characteristic parameters that are an integral part of our formalism. In §4 we present the formal solution to the problem in the three frequency regimes that are characteristic of the dust thermal spectrum, and in §5 we present the joint solution for the SED. In §6 we discuss luminosity conservation and the resultant form of the temperature profile. §7 presents the accuracy and range of applicability of our solution. §8 is dedicated to an explanation of our results and analysis, with particular attention to the shape of the SED and its dependence on two parameters, the feasibility of inferring density profiles from the SED, and the emergent three-component spectrum for highly extended envelopes. In Paper II, we shall present the far-IR SEDs and inferred source and evolutionary parameters for a broad range of sources, from low mass protostars, to massive protostars and ULIRGS.

2. Formulation of the Problem

We consider a centrally concentrated source of radiation surrounded by a homogenous, spherical distribution of dust. Consideration of a central source of radiation, while appropriate for protostellar sources, is approximately valid for ULIRGs, particularly if the far-IR emission is predominantly powered by an extended starburst. As such, our method is more applicable for ULIRGs largely powered by dust-enshrouded AGN or compact star clusters, and for super-star clusters in starburst galaxies and ULIRGs. A relevant finding here is that of Soifer (et al 2000) - they find that that a large fraction of the mid-infrared emission stems from very compact systems. If the source is unresolved, our method is applicable when the dust temperature in the beam is dominated by the central source. If there are multiple sources present, or if the background temperature is significant, then the angular resolution needs to be sufficient to meet the above condition. If the angular resolution of the beam is sufficient to resolve the source, our method can be applied to compute the emergent SED given that all the flux from the source is included in the beam. Our assumption of spherical symmetry limits us to consideration of young protostellar sources in which any accretion disk is small enough with respect to the surrounding envelope that it does not significantly affect the SED. We approximate the density distribution by a power law in radius. We also assume that the dust is homogeneous; the effect of clumping will be considered in a future paper (Chakrabarti & McKee, Paper III).

We neglect scattering of radiation by dust grains and consider only the thermal emission in computing the emergent SED, as the scattering efficiency scales as λ^{-4} and is thus important only at very short wavelengths. We consider dust shells sufficiently opaque that the dust destruction front is highly obscured, and thus does not significantly affect the far-IR spectrum (see Appendix

A). This also implies that the observed SED is independent of the spectrum of the central source of radiation. We consider the opacity to be a function of frequency only; we do not consider the temperature dependence of the opacity that can be caused by evaporation of grains. Although we do not treat the temperature dependence of the opacity explicitly, we give a simple prescription to implement it in Paper II. These assumptions are discussed in more detail in §7.

We find that we get excellent agreement with the numerical solution from DUSTY for the far-IR SED with the adoption of a power law temperature profile. We have specified the variation of the slope of the temperature profile over a parameter space that spans a range of optical depths of a factor of ~ 1000 , through a combination of heuristic arguments and numerical calibration with DUSTY. Thus, although the actual temperature profile is not a pure power law, the mm to far-IR emission can be well described by an effective power-law temperature profile that characterizes the emission coming from close to the Rosseland photosphere. Most of the observed emission originates outside the Rosseland photosphere, since emission at high frequencies is attenuated by the intervening optical depth, and emission at low frequencies comes from outside the $\tau = 1$ surface at the peak of the SED.

As explained in §6, we adopt a temperature profile that is a result of imposing the self-consistency criterion that the input luminosity be equal to the emergent luminosity. We find that, for a given density profile and dust model, the slope of the temperature profile is a function of one dimensionless parameter, insofar as most of the emitted flux is longwards of $\lambda \sim 30 \mu\text{m}$, where the opacity is approximately a power law in frequency.

2.1. Density Profile

Observations of low and high mass star forming regions (Shirley et al 2000, Shirley et al 2002, Beuther et al 2002, Jorgensen et al 2000, van der Tak et al 2000, Mueller et al 2002) have found power law density profiles, $\rho(r) \propto r^{-k_\rho}$, with density power law index, k_ρ , in the range of 1 to 2. As discussed in more detail in §8, within our formalism we approximate $k_\rho = 1$ with $k_\rho = 1.1$, as the emitted spectra agree nearly exactly. We note that most of these authors have found power law density profiles from a combination of fitting to the observed SED and intensity profiles. (We defer detailed discussion of the feasibility of inferring density profiles from the SED alone to §8.) The observed prevalence of power law density profiles in protostellar envelopes can be heuristically understood in the context of a self-similar, turbulent medium (MT03). The self-similarity should be broken only on small scales, by thermal motions (MT03), as they are observed to do in regions of low-mass star formation (Blitz & Williams 1997). However, such a picture of a time-stationary, spherical, self-gravitating turbulent structure is necessarily highly approximate, and large fluctuations, both spatial and temporal, are to be expected. We defer consideration of these fluctuations, which correspond to clumpiness, to a future paper.

It is important to note that the observations of massive star forming regions cited above probed

scales of *clumps*, which are massive enough to form a cluster of stars, rather than of *cores*, which will form a single star or binary. (We follow the clump-core terminology introduced in Williams, Blitz & McKee 2000.) However, as we shall show in Paper II, the photosphere of a high-mass protostar is within its natal core. Cores are too small to have measured density profiles yet. We assume that they also have power-law density profiles, which is consistent with MT03’s assumption that clumps and cores are part of a self-similar structure. We assume that the cores have a definite outer radius at R_c , beyond which the density drops rapidly; we assume that the emission from beyond R_c is negligible.

While the simplest SED models of star-forming galaxies do not consider a density variation (e.g. YC02), more sophisticated radiative transfer models (Efstathiou et al 2000) have considered starburst galaxies as an ensemble of optically thick clouds heated by the newly formed stars. The assumption of power-law density profiles for ULIRGs is a very approximate representation of the complex morphology of merging systems; it may be a good approximation for the clouds that comprise the ULIRGs, however.

2.2. Dust Opacity

The results presented in this paper are based on the Weingartner & Draine (2001) (henceforth WD01) $R_V = 5.5$ dust model. WD01 is an extension of the original Draine & Lee (1984) dust model, with a size distribution developed to reproduce the observed extinction curve for a variety of environments, parametrized by the ratio of the visual extinction to reddening, R_V . For the diffuse ISM, R_V is observed to be approximately 3. Higher values have been observed for dense clouds (Strafella et al 2001, Kandori et al 2003, Vrba et al 1993) and star-forming galaxies (Calzetti 2000).

The WD01 model has a simple composition, consisting of carbonaceous grains and silicates. WD01’s $R_V = 5.5$ model has a substantial depletion of the smallest carbonaceous grains relative to the $R_V = 3.1$ model, leading to a difference in the opacity curves in the near-IR. However, WD01’s best fit models for $R_V = 5.5$ and $R_V = 3.1$ have no difference in the far-IR extinction curves, and thus imply no substantial grain growth for sizes on the large end of the size distribution, i.e., $a \sim 0.1 \mu\text{m}$. As we later show, for densities typical of protostellar regions and dusty galaxies, it is unlikely that significant coagulation occurs within a few free-fall times to affect the spectrum in the mm to far-IR region of the spectrum. For uncoagulated grain models such as WD01, the mm to far-IR variation of the opacity with frequency (in the range of 3 mm to 30 μm) is well represented as a power law with slope, $\beta = 2$.

The opacity normalization per gram of dust, κ_{ν_0} , depends on the metallicity. Let Z_d be the mass fraction of dust, equal to 1/105.1 for solar abundances (WD01) and δ be the dust-to-gas ratio relative to solar. At a fiducial wavelength of $\lambda_0 = 100 \mu\text{m}$, WD01’s opacity is $\kappa_{\nu_0} = 0.27\delta$, independent of R_V . The WD01 models reproduce the observed extinction curves for the Milky

Way, as well as regions of low metallicity, such as the LMC and the SMC. Since WD01 is the simplest grain model that is able to reproduce the observed extinction over a wide range of metallicities, we have adopted it as our fiducial dust model.

The principal omission in the WD01 model is the lack of ice mantles. Spectroscopic studies have identified ice spectral features in protostellar environments and in dusty galaxies (Allamandola et al 1992, Tielens et al 1984, Spoon et al 2002). Based on observations with the Submillimeter Wave Astronomy Satellite, Bergin et al. (2000) have argued that most of the oxygen in star-forming regions is frozen out onto the dust grains in the form of molecular ices. Preibisch et al. (1993) have modeled dirty ice mantles, and find significant variations in the opacity, depending on how the mantles are distributed among the grains and on the volume fraction of carbonaceous material; a typical increase in the far-infrared opacity is a factor ~ 2 . Pollack et al (1994) considered detailed grain compositions, including the contribution from water ice. If most of the oxygen is in the form of water ice, they find that $\kappa_{\nu_0} \simeq 1 \text{ cm}^2 \text{ g}^{-1}$ at $100 \mu\text{m}$; however, at $\lambda_0 = 1 \text{ mm}$, the opacity for spherical grains of average radius $1 \mu\text{m}$ is $4.2 \times 10^{-3} \text{ cm}^2 \text{ g}^{-1}$, not that different from WD01 ($\kappa_{\nu_0} = 3.0 \times 10^{-3} \text{ cm}^2 \text{ g}^{-1}$). However, the steep power law index for the opacity, $\beta = 2.7$, found by Pollack et al. does not appear to be consistent with observations. Pollack et al. show that for typical conditions in regions of high-mass star formation ($n_H \sim 10^6 \text{ cm}^{-3}$), ice sublimates at $T \simeq 110 \text{ K}$. We conclude that significant uncertainties remain in the effect of ice mantles on the far-infrared opacity. We show later in §3 that the effective increase in opacity normalization that ice mantles produce may be simply treated within our formalism.

A further complication to consider is the possible growth of grains due to coagulation (Pollack et al. 1994; Ossenkopf & Henning 1994). The time scale for coagulation depends on the mean relative speed of the grains, which is likely due by turbulence (Draine 1985; Lazarian & Yan 2002) in dense cores. The outcome of a collision between grains depends on whether or not the grains stick together, i.e., if the surface potential energy is comparable to or larger than the kinetic energy. Recent numerical experiments (Poppe et al 2000) have shown that relative velocities of order 1 m/s allow sticking probability of order unity, with a sharp decline at $v \sim 5 \text{ m/s}$. Therefore, the timescale for grain coagulation is approximately

$$t_{\text{coag}} \sim \frac{1}{n\sigma v_{\text{rel}}} = 6 \times 10^6 \text{ yr} \left(\frac{10^5 \text{ cm}^{-3}}{n_H} \right) \left(\frac{a}{0.1 \mu\text{m}} \right) \left(\frac{1 \text{ m s}^{-1}}{v_{\text{rel}}} \right), \quad (1)$$

where we have considered the approximate case of coagulation of identical, spherical grains of size a . To determine whether coagulation will be effective within timescales relevant for protostellar evolution, we compare this coagulation time scale to the free fall time. For coagulation to affect the spectrum in the far-IR range would require grain growth to the Rayleigh limit, i.e., to sizes $a \sim \lambda/2\pi$, $a \gtrsim 5 \mu\text{m}$, (to affect emission at $\lambda \gtrsim 30 \mu\text{m}$). This gives:

$$\frac{t_{\text{coag}}}{t_{\text{ff}}} \sim 2000 \left(\frac{10^5 \text{ cm}^{-3}}{n_H} \right)^{1/2} \left(\frac{a}{5 \mu\text{m}} \right) \left(\frac{1 \text{ m s}^{-1}}{v_{\text{rel}}} \right). \quad (2)$$

Therefore, for typical estimates of the densities, $n_H \sim 10^6 \text{ cm}^{-3}$, we see that the coagulation timescale is more than several hundred times the free-fall time for $a \sim 5 \mu\text{m}$, which corresponds to

$\lambda = 30\mu\text{m}/2\pi$. This conclusion is consistent with the results of Chokshi et al. (1993), who found a relatively small increase in grain size (approximately a factor of 2) in dense cores. We conclude that coagulation in star-forming regions is unlikely to significantly alter the far-infrared opacity.

3. Characteristic Parameters

Stars have well-defined photospheres, but dust clouds do not. Nonetheless, the SED of a dusty source can be described in terms of characteristic radius, R_{ch} , and characteristic temperature, T_{ch} , such that

$$L \equiv 4\pi \tilde{L} R_{\text{ch}}^2 \sigma T_{\text{ch}}^4, \quad (3)$$

where \tilde{L} is a number of order unity determined below in order to secure better agreement with the actual SED. We determine R_{ch} and T_{ch} by requiring that a characteristic optical depth at frequency $\nu_{\text{ch}} \equiv kT_{\text{ch}}/h$ is unity,

$$\tau_{\text{ch}} = \kappa_{\text{ch}} \int_1^{R_c \rightarrow \infty} \rho(\tilde{r}) d\tilde{r} = \frac{\kappa_{\nu_{\text{ch}}} \rho(R_{\text{ch}}) R_{\text{ch}}}{k_{\rho} - 1} = 1; \quad (4)$$

note this characteristic optical depth ignores the cut off in the density at the edge of the cloud, which is at R_c . R_{ch} and T_{ch} are therefore the approximate photospheric radius and temperature; more accurate photospheric values are given in §7 below.

We now express the characteristic parameters in terms of the physical source parameters, the surface mass density, $\Sigma \equiv M/\pi R^2$, and the luminosity to mass ratio, L/M . We assume that ν_{ch} lies within the frequency regime in which the opacity is a power law,

$$\kappa_{\nu} = \kappa_{\nu_0} (\nu/\nu_0)^{\beta} \quad (30 \mu\text{m} \lesssim \lambda \lesssim 1 \text{ mm}). \quad (5)$$

Solving equations (3) and (4), we evaluate the two parameters that we use to describe our solutions,

$$\tilde{R}_c \equiv \frac{R_c}{R_{\text{ch}}} = \left\{ \frac{(L/M) \Sigma^{(4+\beta)/\beta}}{4\sigma \tilde{L}} \left[\frac{(3-k_{\rho}) \kappa_{\nu_0}}{4(k_{\rho}-1) T_0^{\beta}} \right]^{4/\beta} \right\}^{-\frac{\beta}{2\beta+4(k_{\rho}-1)}}, \quad (6)$$

and

$$T_{\text{ch}} = \left\{ \frac{L/M}{4\sigma \tilde{L} \Sigma^{\frac{3-k_{\rho}}{k_{\rho}-1}}} \left[\frac{4(k_{\rho}-1) T_0^{\beta}}{(3-k_{\rho}) \kappa_{\nu_0}} \right]^{\frac{2}{k_{\rho}-1}} \right\}^{\frac{k_{\rho}-1}{2\beta+4(k_{\rho}-1)}}. \quad (7)$$

In general, \tilde{L} is a function of \tilde{R}_c , the form of which is specified in §6. It is important to note that while we have defined the characteristic parameters in terms of a power law opacity for simplicity, our solution for the emergent SED is valid for an arbitrary opacity curve, as we show later.

The utility of equations (6) and (7) is to allow an analytic translation between the SED variables, \tilde{R}_c and T_{ch} , which govern the shape of the SED, and the source parameters, L/M and Σ .

The luminosity-to-mass ratio and the surface density are independent of distance, and therefore, the SED variables, \tilde{R}_c and T_{ch} , are also. Once the SED variables are determined from two observed color ratios, we may then immediately solve for L/M and Σ using these equations.

The SED variable $\tilde{R}_c = R_c/R_{\text{ch}}$ is a dimensionless measure of the size of the region that the observed far-IR SED probes. When it is large, the observed emission arises from a wide range of radii; when it is somewhat larger than unity, the emission comes from a narrow range. Values of \tilde{R}_c less than unity are generally not meaningful since the resulting spectrum is sensitive to our assumption that the emission at $r > R_c$ drops to zero. As we shall see below, dense dust shells, such as those characteristic of massive protostars, starbursts and AGN, have smaller values of \tilde{R}_c than lower density dust shells, such as those characteristic of low-mass protostellar envelopes. Thus, for low-mass protostellar envelopes, we probe the source function over a larger region than for high-mass envelopes.

The angular size of the photosphere is about

$$\theta_{\text{ch}} \equiv \frac{R_{\text{ch}}}{D}, \quad (8)$$

where D is the distance to the source. If the total flux, $F \equiv L/4\pi D^2$, is known, then the angular size is

$$\theta_{\text{ch}} = \left(\frac{F}{\tilde{L}\sigma T_{\text{ch}}^4} \right)^{1/2} \quad (9)$$

from equation (3). Thus, since T_{ch} determines the surface brightness of the source, it is possible to infer the angular size of the source even if it is unresolved. If the distance to the source is also known, we may then further solve for the size of the source, as well as the mass and luminosity.

In Figure 1a, we have depicted the typical locations of various sources on the L/M vs Σ plot. Isolated low-mass protostars appear typically on the lower left corner of this diagram, i.e., at low surface density, $\Sigma \sim 0.05 \text{ g cm}^{-2}$, and low luminosity to mass ratios, $L/M \sim 1 L_{\odot}/M_{\odot}$ (Jorgensen et al 2002). In clusters, Σ is higher since the pressures are higher (MT03). High-mass protostars, ULIRGs and super-star clusters are typically in regions of higher surface density, $\Sigma \sim 1 \text{ g/cm}^2$ (Plume et al 1997, MT03), and thus appear on the right-hand side of this diagram. ULIRGs and super-star clusters have comparable $L/M \sim 10 L_{\odot}/M_{\odot}$ on average (Downes & Solomon 1998), (Gilbert & Graham 2002, Gilbert 2002). Two sets of lines of constant T_{ch} and \tilde{R}_c are overlaid on this diagram for our fiducial density profile, $k_{\rho} = 3/2$, and our adopted dust model WD01. As discussed above, ice-coated grains produce an effective change in the opacity normalization of a factor of ~ 2 . Our scaling relations (6) and (7) show that this leads to a small change in the governing SED variables. The difference relative to WD01's normalization when ice-coated grains are considered is depicted in Figure 1b for our fiducial density profile. A more quantitative discussion of the characteristic parameters is relegated to §7. Figures 2a, b, and c present fits to observed data for a low, high-mass protostar and ULIRG, respectively. Paper II gives a detailed explanation of the application of our methodology to star-forming system, along with SED fits to about a dozen sources, from low-mass protostars to ULIRGs.

4. Evaluation of L_ν

We compute the spectral luminosity as

$$L_\nu = 4\pi \int_{R_{\text{dd}}}^{R_c} j_\nu f_\nu(r) 4\pi r^2 dr , \quad (10)$$

where j_ν is the emissivity and $f_\nu(r)$ is the escape probability, which is evaluated in Appendix B. The inner boundary of the emitting shell is at R_{dd} , the dust destruction radius, and the outer boundary is at R_c , the radius of the cloud. At high densities, the dust and gas temperatures are the same, but at low densities they may differ; in our equations, T always refers to the dust temperature. We assume that the dust emissivity is given by the LTE expression, $j_\nu = \kappa_\nu \rho(r) B_\nu(T)$. This approximation breaks down at the dust destruction front, where the absorption of UV photons can lead to transient heating of small grains (Draine & Anderson 1985). However, since we assume that the cloud is sufficiently opaque that the dust destruction front is shielded from view, the LTE approximation should be valid.

In order to evaluate the luminosity, we must specify the temperature profile. We assume that it can be approximated as a power law in the vicinity of the photosphere,

$$T = T_{\text{ch}} \left(\frac{r}{R_{\text{ch}}} \right)^{-k_T} = T_{\text{ch}} \tilde{r}^{-k_T} , \quad (11)$$

where $\tilde{r} \equiv r/R_{\text{ch}}$. We determine k_T to zeroth-order by imposing the self-consistency condition that the input luminosity equal the emergent luminosity - the procedure is described in detail in §6. Note that this assumed form for the temperature carries the implicit assumption that the temperature at R_{ch} is T_{ch} ; we choose $\tilde{L}(\tilde{R}_c)$ choose so as to improve the accuracy of this approximation. Written in dimensionless notation, our expression for the luminosity then becomes

$$L_\nu = 4\pi R_{\text{ch}}^2 4\pi \left(\frac{2h\nu_{\text{ch}}^3}{c^2} \right) \tilde{\kappa}_\nu \tilde{\nu}^3 (k_\rho - 1) I , \quad (12)$$

where

$$I = \int_{R_{\text{dd}}}^{R_c} \frac{f_\nu(\tilde{r}) \tilde{r}^{2-k_\rho}}{\exp(\tilde{\nu} \tilde{r}^{k_T}) - 1} d\tilde{r} , \quad (13)$$

$\tilde{\nu} \equiv \nu/\nu_{\text{ch}}$, $\tilde{\kappa}_\nu \equiv \kappa_\nu/\kappa_{\nu_{\text{ch}}}$, and $h\nu/kT(r) = \tilde{\nu} \tilde{r}^{k_T}$. Note that since the integral is performed over position, we may take the opacity term, κ_ν , outside the integral since we have assumed the opacity is not a function of position.

In order to obtain an approximate analytic evaluation of I , we have found it necessary to consider three distinct frequency regimes, which we denote as low, intermediate, and high. The low and intermediate frequencies are optically thin. Low frequencies are in the Rayleigh-Jeans portion of the spectrum throughout the envelope [$h\nu < kT(R_c)$]. The low-frequency emission comes predominantly from the outer parts of the shell, as it is proportional to the mass. Intermediate frequencies are in the Wien portion of the spectrum in the outer envelope, although not near the

photosphere. The temperature dependence of the intermediate frequency region causes the higher components of this frequency regime to emanate from deeper in the envelope, in a sense specified by the temperature variation of the envelope. High-frequencies are in the Wien portion of the spectrum at the photosphere; the emission originates from a location that is due to a tug-of-war between the hotter temperature in the interior and the intervening optical depth that has to be traversed.

Once we obtain an approximate expression for L_ν in each of these frequency regimes, it is necessary to knit them together into a single expression. To do this, we have found it convenient to introduce a “shell” model, in which the emission at each frequency comes from a shell of thickness $\Delta r_m(\nu)$ centered at a radius $r_m(\nu)$, with a source function $(2h\nu_{ch}^3/c^2) \exp[-h\nu/kT(\tilde{r}_m)]$ located at an optical depth $\tau_\nu(\tilde{r}_m)$:

$$L_\nu = 4\pi R_{ch}^2 4\pi \left(\frac{2h\nu_{ch}^3}{c^2} \right) \tilde{\kappa}_\nu \tilde{\nu}^3 (k_\rho - 1) \tilde{r}_m^{2-k_\rho} \Delta \tilde{r}_m \exp \left[-\frac{h\nu}{kT(\tilde{r}_m)} - \tau_\nu(\tilde{r}_m) \right], \quad (14)$$

where the optical depth τ_ν from r to the surface of the cloud is

$$\tau_\nu = \tilde{\kappa}_\nu \left(\tilde{r}^{-k_\rho+1} - \tilde{R}_c^{-k_\rho+1} \right). \quad (15)$$

We now proceed to evaluate the parameters of this intuitively transparent form for the spectral luminosity.

4.1. Low and Intermediate Frequency Regimes ($\tau_\nu \ll 1$)

The low and intermediate frequency regimes are characterized by $\tau_\nu \ll 1$, so that the escape fraction is approximately unity, $f_\nu(\tilde{r}) \simeq 1$. Low frequencies are in the Rayleigh-Jeans part of the spectrum throughout the cloud, so that $h\nu/kT = \tilde{\nu}\tilde{r}^{k_T} \ll 1$ everywhere and the exponential in I can be expanded,

$$I_{\text{low}} = \frac{\tilde{R}_c^{3-k_\rho-k_T}}{(3-k_\rho-k_T)\tilde{\nu}}, \quad (16)$$

where we have assumed that $R_{dd}^{3-k_\rho-k_T} \ll R_c^{3-k_\rho-k_T}$, so that the dust destruction radius does not significantly affect the spectrum; equivalently, the emission is dominated by the outer part of the envelope. We note that this requires $k_T < 3 - k_\rho$.

Intermediate frequencies are in the Wien part of the spectrum in the outer part of the cloud ($h\nu/kT(R_c) \gg 1$), and as a result the upper limit integration can be set to infinity. Since we have assumed that the dust destruction front does not affect the spectrum, we then find

$$I_{\text{int}} = \Gamma \left(\frac{3-k_\rho}{k_T} \right) \zeta \left(\frac{3-k_\rho}{k_T} \right) \frac{1}{k_T \tilde{\nu}^{(3-k_\rho)/k_T}} \quad (17)$$

(Gradshteyn & Ryzhik p. 349).

Now we combine the formal expressions for the low and intermediate frequency fluxes into a single expression by observing the scaling behavior of each. In this case, we require a harmonic mean to recover each limiting case, $I_{\text{low-int}}^{-1} = I_{\text{low}}^{-1} + I_{\text{int}}^{-1}$. The resulting expression for the luminosity is

$$L_{\nu, \text{low-int}} \simeq 16\pi^2(k_\rho - 1) \left(\frac{2h\nu_{\text{ch}}^3}{c^2} \right) \tilde{\kappa}_\nu R_{\text{ch}}^2 \tilde{\nu}^3 \left[\frac{\Gamma\zeta}{(3 - k_\rho - k_T)\tilde{\nu}\Gamma\zeta\tilde{R}_c^{-(3-k_\rho-k_T)} + k_T\tilde{\nu}^{(3-k_\rho)/k_T}} \right], \quad (18)$$

where the argument $(3 - k_\rho)/k_T$ for the Gamma and Zeta functions has been suppressed for clarity. This prescription holds for k_ρ in the range of 1 to 2 that we are considering.

Recall that in our shell model (eq. 14), we characterize the emission at each frequency as coming from an optically thin shell centered at a radius $r_m(\nu)$ and having width $\Delta r_m(\nu)$. To apply this equation, we must determine the shell radius and thickness. The shell radius r_m is also known as the contribution function (e.g., Gray p. 278). As discussed below equation (16), most of the low-frequency emission comes from the outer part of the shell, so we set $\tilde{r}_{m, \text{low}} = \tilde{R}_c$. To determine the shell radius at intermediate frequencies, we assume that $h\nu/kT(\tilde{r}_{m, \text{int}})$ is a constant,

$$\frac{h\nu}{kT(\tilde{r}_{m, \text{int}})} = \tilde{\nu}\tilde{r}_{m, \text{int}}^{k_T} = C, \quad (19)$$

where C is determined from numerical calibration in §7 and §8.1. To recover the limiting cases, the shell radius for both low and intermediate frequencies can be approximated by the harmonic mean, so that

$$\tilde{r}_{m, \text{low-int}} = \frac{\tilde{R}_c C^{1/k_T}}{\tilde{R}_c \tilde{\nu}^{1/k_T} + C^{1/k_T}}, \quad (20)$$

As we discuss in detail in §8.1, when $\tilde{r}_{m, \text{low}} = \tilde{r}_{m, \text{int}}$, the slope of the emitted spectrum changes from the standard Rayleigh-Jeans slope to the flatter intermediate frequency slope. This break frequency, i.e., the frequency at which the character of the emission changes from being dominated by the cool material on the outside to the emission coming from deeper into the envelope in a sense specified by the temperature gradient, is then given by:

$$\tilde{\nu}_{\text{break}} = C\tilde{R}_c^{-k_T}. \quad (21)$$

In terms of the temperature at the outer edge of the envelope, the break frequency is:

$$\nu_{\text{break}} = \frac{kT(R_c)}{h}. \quad (22)$$

In order to recover equation (18) for the luminosity at low and intermediate frequencies, we must set the thickness of this emitting region to be

$$\Delta\tilde{r}_m = \left[\frac{\Gamma\zeta e^{h\nu/kT(\tilde{r}_{m, \text{low-int}})}}{(3 - k_\rho - k_T)\tilde{\nu}\Gamma\zeta\tilde{R}_c^{-(3-k_\rho-k_T)} + k_T\tilde{\nu}^{(3-k_\rho)/k_T}} \right] \frac{1}{\tilde{r}_{m, \text{low-int}}^{2-k_\rho}}. \quad (23)$$

4.2. High-Frequency Regime

In the high-frequency regime, the optical depth can be larger than unity and it is necessary to develop an escape fraction appropriate for spherical geometry. In Appendix B we show that an appropriate escape fraction for spherical geometry is:

$$f(\tilde{r}) \simeq \frac{e^{-\tau_\nu}}{1 + 2\tilde{\kappa}_\nu \left(\frac{k_\rho - 1}{k_\rho + 1} \right) \left(\tilde{r}^{1-k_\rho} - \tilde{r}^2 \tilde{R}_c^{-k_\rho-1} \right)}, \quad (24)$$

where τ_ν is the radial optical depth and is given in equation (15). We note that for a given dust model and density profile, the optical depth depends on T_{ch} in a scale-free manner so long as we consider wavelengths longwards of $30 \mu\text{m}$, where $\kappa_\nu \propto \nu^p$ is a power-law in frequency.

We compute the high-frequency luminosity by the method of steepest descent. This method is particularly useful when the integrand is composed of a rapidly varying function and a slowly varying function, such as an exponential term multiplied by an algebraic term, which is indeed the structure of the high-frequency integrand. The method of steepest descent approximates the integral as the algebraic term evaluated at the local maximum of the exponential and a gaussian centered at the local maximum, having a width that is proportional to the second derivative of the argument of the exponential. The narrowness of this gaussian is an indication of how local the contribution to the integrand really is. The narrower the gaussian, the better the approximation.

Inserting our expression for the escape fraction into equations (12) and (13) we find

$$L_\nu = 16\pi^2(k_\rho - 1)R_{\text{ch}}^2 \tilde{\kappa}_\nu \tilde{\nu}^3 \left(\frac{2h\nu_{\text{ch}}^3}{c^2} \right) \int_0^\infty \frac{\tilde{r}^{2-k_\rho} e^{-h(\tilde{r})}}{1 + 2\tilde{\kappa}_\nu \left(\frac{k_\rho - 1}{k_\rho + 1} \right) \left(\tilde{r}^{1-k_\rho} - \tilde{r}^2 \tilde{R}_c^{-k_\rho-1} \right)} d\tilde{r}. \quad (25)$$

where the argument of the exponential term is

$$h(\tilde{r}) = \tilde{\nu} \tilde{r}^{k_T} + \tilde{\kappa}_\nu \left(\tilde{r}^{1-k_\rho} - \tilde{R}_c^{1-k_\rho} \right). \quad (26)$$

The location of the maximum of the exponential term [i.e., the minimum of $h(\tilde{r})$] gives the shell radius at high frequencies according to the method of steepest descent,

$$\tilde{r}_{m, \text{high, steep}} = \left[\frac{\tilde{\kappa}_\nu (k_\rho - 1)}{\tilde{\nu} k_T} \right]^{1/(k_T + k_\rho - 1)}. \quad (27)$$

Physically, this means that the high-frequency photons come from a location in the shell that is due to a competition between the optical depth and the temperature gradient, with the temperature gradient driving $\tilde{r}_m(\nu)$ inwards, while the optical depth drives $\tilde{r}_m(\nu)$ outwards.

In principle, this expression for the shell radius can give $\tilde{r}_{m, \text{high}} > \tilde{R}_c$, whereas in fact $\tilde{r}_m \rightarrow \tilde{R}_c$ as the shell envelope becomes very opaque. Thus, in general the shell radius is given by

$$\tilde{r}_{m, \text{high}} = \text{Min}(\tilde{R}_c, \tilde{r}_{m, \text{high, steep}}). \quad (28)$$

It is important to note that, in finding the contribution function for the high-frequency regime, we made no assumption about the frequency dependence of the opacity curve, and thus we may use a tabulated, realistic opacity curve to find \tilde{r}_m for the high-frequency regime. We have assumed that κ_ν is independent of position for simplicity, but in principle equation (27) could be generalized to include temperature dependent opacity, $\kappa_\nu[T(r)]$.

Evaluating the integral in equation (25) by the method of steepest descent, we find

$$L_{\nu, \text{high}} = 16\pi^2(k_\rho - 1)R_{\text{ch}}^2\tilde{\kappa}_\nu\tilde{\nu}^3 \left(\frac{2h\nu_{\text{ch}}^3}{c^2} \right) \frac{\tilde{r}_{m, \text{high}}^{2-k_\rho}(2\pi/h_m'')^{1/2}e^{-h_m}}{1 + 2\tilde{\kappa}_\nu \left(\frac{k_\rho-1}{k_\rho+1} \right) (\tilde{r}_{m, \text{high}}^{1-k_\rho} - \tilde{r}_{m, \text{high}}^2 \tilde{R}_c^{-k_\rho-1})}, \quad (29)$$

where $h_m \equiv h(\tilde{r}_{m, \text{high}})$ and

$$h_m'' = \tilde{\nu}k_T(k_T - 1)\tilde{r}_{m, \text{high}}^{k_T-2} + k_\rho(k_\rho - 1)\tilde{\kappa}_\nu\tilde{r}_{m, \text{high}}^{-k_\rho-1}. \quad (30)$$

We can express the luminosity in the form of the shell model (eq. 14) if we identify the thickness as

$$\Delta\tilde{r}_{m, \text{high}} = \frac{(2\pi/h_m'')^{1/2}}{1 + 2\tilde{\kappa}_\nu \frac{(k_\rho-1)}{k_\rho+1} \left(\tilde{r}_{m, \text{high}}^{1-k_\rho} - \tilde{r}_{m, \text{high}}^2 \tilde{R}_c^{-k_\rho-1} \right)}. \quad (31)$$

The width of the high-frequency gaussian is given by $(2/h_m'')^{1/2}$. We require $h_m'' > 1$ for proper application of steepest descent. This condition breaks down at lower frequencies, but we avoid this problem by combining the high-frequency results with the low and intermediate ones. We also note that one can show from eqn. (29) that our high frequency expression has a “super-Wien” behavior, i.e., it falls off faster than $\nu^3 \exp(-h\nu/kT)$.

5. Joint Spectrum

To construct a joint spectrum that is valid in all three frequency regimes, we use the shell model. In order to recover the limiting cases for the shell radius and thickness, we sum the results from the low-intermediate and high frequencies,

$$\tilde{r}_m = \text{Min} \left\{ \frac{\tilde{R}_c C^{1/k_T}}{\tilde{R}_c \tilde{\nu}^{1/k_T} + C^{1/k_T}} + \left[\frac{(k_\rho - 1)\tilde{\kappa}_\nu}{\tilde{\nu}k_T} \right]^{1/(k_\rho + k_T - 1)}, \tilde{R}_c \right\}, \quad (32)$$

$$\begin{aligned} \Delta\tilde{r}_m = & \left[\frac{\Gamma\zeta \exp\left(\tilde{\nu}\tilde{r}_{m, \text{low-int}}^{k_T}\right)}{(3 - k_\rho - k_T)\tilde{\nu}\Gamma\zeta\tilde{R}_c^{-(3-k_\rho-k_T)} + k_T\tilde{\nu}^{(3-k_\rho)/k_T}} \right] \frac{1}{\tilde{r}_{m, \text{low-int}}^{2-k_\rho}} \\ & + \frac{(2\pi/h_m'')^{1/2}}{1 + 2\tilde{\kappa}_\nu \left(\frac{k_\rho-1}{k_\rho+1} \right) (\tilde{r}_{m, \text{high}}^{1-k_\rho} - \tilde{r}_{m, \text{high}}^2 \tilde{R}_c^{-k_\rho-1})}, \end{aligned} \quad (33)$$

How do these results behave in the limiting cases of very extended ($\tilde{R}_c \rightarrow \infty$) and very compact ($\tilde{R}_c \rightarrow 0$) envelopes? For extended envelopes, the break frequency, $\nu_{\text{break}} \rightarrow 0$, so that the low-frequency regime disappears. Correspondingly, the shell radius at low and intermediate frequencies approaches the intermediate value, $\tilde{r}_{m,\text{int}} \rightarrow (C/\nu)^{1/k_T}$. The high-frequency emission changes in this limit only insofar as τ_ν increases somewhat.

In the opposite limit of large optical depths, ($R_{\text{ch}} \rightarrow \infty$, so that $\tilde{R}_c \rightarrow 0$), the photosphere approaches the cloud surface and the slope of the temperature profile becomes very steep ($k_T \gg 1$). This case is difficult to realize in practice since we have assumed that there is no emission beyond R_c , and it is difficult, though not impossible, to realize such sharp boundaries in practice. A possible example of such a sharp boundary is a photoevaporating globule (Bertoldi & McKee 1990). We do not attempt to treat the $\tilde{R}_c \rightarrow 0$ limit in this paper, but instead confine our attention to $\tilde{R}_c \gtrsim 1$.

Figure 3a depicts the analytic SED (crosses) overplotted on the numerical SED (solid line) produced from DUSTY, with the three frequency regimes marked on the plot. This is a typical SED from the region of the physical parameter space labeled as “high mass protostar” in Figure 1, with $L/M \sim 400L_\odot/M_\odot$ and $\Sigma \sim 1 \text{ g cm}^{-2}$. Figure 3b shows the combined contribution function. Figure 3c is a plot of the opacity curve, WD01’s $R_V = 5.5$. One should read these three plots left to right, i.e., follow the marked regions in the SED plot in Figure 3a and correlate them with the marked regions in the contribution function in Figure 3b. The spectral features in the contribution function in Figure 3b correlate with the spectral features in the opacity curve as depicted in Figure 3c. For example, the $10 \mu\text{m}$ ($3 \times 10^{13} \text{ Hz}$) increase in the opacity translates to a corresponding increase in \tilde{r}_m , as the $\tau = 1$ surface at this frequency is driven outwards, while the $5 \mu\text{m}$ ($6 \times 10^{13} \text{ Hz}$) decrease in the opacity causes \tilde{r}_m to move inwards.

6. Temperature Profile

Numerical radiative transfer schemes solve for the temperature profile within the envelope by enforcing the condition of radiative equilibrium within every resolution element, i.e., that the total energy absorbed by a differential volume element equal the total energy emitted. This condition of energy balance is equivalent to the condition of zero flux divergence when the radiation field is time-independent (Mihalas, p.48). In particular, in spherical geometry, this condition is equivalent to the constancy of luminosity as a function of radius. Approximate numerical radiative transfer schemes, such as that of Adams & Shu (1985), have enforced radiative equilibrium at a discrete number of points, using a particular form of the temperature profile, and shown that the total luminosity transported is approximately constant as a function of radius. Subsequently, more precise numerical radiative transfer solutions have solved for the temperature variation in the envelope in full generality, and enforced radiative equilibrium at fine resolution intervals, thereby guaranteeing virtually exact constancy of luminosity (IE97).

Here, in our analytic treatment of the radiative transfer problem, we have found that the far-

IR emission can be inferred with good accuracy from a single power-law temperature profile. We determine the slope of this temperature profile from the self-consistency condition that the input luminosity exactly equal the emergent luminosity:

$$L \equiv 4\pi R_{\text{ch}}^2 \sigma T_{\text{ch}}^4 \tilde{L} \equiv \int L_\nu d\nu . \quad (34)$$

Inserting the shell expression for L_ν (eq. 14) into this expression gives

$$\tilde{L}(\tilde{R}_c, T_{\text{ch}}, k_\rho) \equiv \frac{60(k_\rho - 1)}{\pi^4} \int \tilde{\kappa}_\nu \tilde{\nu}^3 \tilde{r}_m^{2-k_\rho} \Delta \tilde{r}_m \exp \left[-\frac{h\nu}{kT(\tilde{r}_m)} - \tau_\nu(r_m) \right] d\tilde{\nu} . \quad (35)$$

This is analogous to requiring constancy of luminosity at two discrete spatial points; numerical schemes achieve greater accuracy by iteratively imposing zero flux divergence over fine resolution elements. Since \tilde{r}_m and $\Delta \tilde{r}_m$ depend on both k_T and C , this equation gives a zeroth-order, self-consistent determination of the slope of the temperature profile, k_T , when the fitting parameters \tilde{L} and C are taken to be equal to unity. To secure better agreement with the numerical results from DUSTY, we have simultaneously solved for k_T , \tilde{L} , and C by imposing (35), and required that the maximum difference between the analytic and numerical SEDs between 3 mm and 30 μm be as small as possible. Two of these parameters (k_T and \tilde{L}) characterize the temperature profile and one (C) determines the break frequency separating low and intermediate frequencies. We find that the parameters \tilde{L} and C are indeed of order unity.

For a given dust opacity, the shape of the SED, and therefore the values of the three fitting parameters, depend on three source parameters, \tilde{R}_c , T_{ch} and k_ρ . The dependence on T_{ch} arises from the opacity, κ_ν . We now recall that the opacity is scale-free longwards of 30 μm . If most of the flux is emitted longwards of 30 μm (corresponding to $h\nu/k = 480\text{K}$), then $\tau_\nu \propto \tilde{\kappa}_\nu = \tilde{\nu}^p$ from equation (15). In order to have most of the flux emitted longwards of 30 μm , we require $T_{\text{ch}} \lesssim 300\text{ K}$ (for $k_\rho = 1.1$, the condition is more stringent, $T_{\text{ch}} \lesssim 250\text{ K}$). For lower values of T_{ch} , the power law approximation to the opacity is valid and our fitting parameters will be independent of T_{ch} . By comparing with DUSTY, we have found that it is possible to further simplify the functional dependences to

$$k_T = k_T(\tilde{R}_c, k_\rho), \quad \tilde{L} = \tilde{L}(\tilde{R}_c), \quad \text{and} \quad C = C(k_\rho) . \quad (36)$$

With these dependences, we find an excellent level of agreement between our analytic results and the numerical results from DUSTY over a parameter space that spans low-mass protostars to ULIRGs.

How do we expect k_T and \tilde{L} to depend on \tilde{R}_c ? We may heuristically understand the functional form of k_T by considering the equation of radiative equilibrium, which requires that dust grains radiate as much as they absorb:

$$\int \kappa_\nu B_\nu d\nu = \int \kappa_\nu J_\nu d\nu , \quad (37)$$

where B_ν is the Planck function and J_ν is the mean intensity of the radiation field.

First consider the outer envelope, assumed to be optically thin. Insofar as we can make the approximation $\kappa_\nu \propto \nu^\beta$ in the LHS of this equation, it scales as $T^{4+\beta}$; the RHS scales as $1/r^2$ in the limit of negligible optical depths. Therefore, in the outer parts of extended, optically thin envelopes, we have $T(r) \propto r^{-2/(4+\beta)}$. If the envelope is cool ($T_{\text{ch}} \lesssim 100$ K), we have $p \simeq 2$ so that the slope of the temperature profile $\rightarrow \frac{1}{3}$. In fact, extended envelopes, which have large values of \tilde{R}_c , generally have higher temperatures, so that the effective value of p is somewhat less than 2 and the slope is somewhat greater than $\frac{1}{3}$. Next consider the inner, opaque region of the envelope. There the diffusion approximation is appropriate, and it gives $T(r) \propto r^{-(1+k_\rho)/(4-\beta)}$, which is steeper than the slope in the outer envelope. For very opaque envelopes, the gradient can become steeper than this near the photosphere, just as in the case of a stellar atmosphere. We wish to choose a single power law, k_T , to represent the temperature gradient near and outside the photosphere. For extended envelopes (large \tilde{R}_c) we expect k_T to approach $2/(4+\beta)$, whereas for compact envelopes (small \tilde{R}_c) we expect k_T to increase as \tilde{R}_c decreases. We find that this expected variation can be represented by the sum of two inverse power laws,

$$k_T = \frac{A}{\tilde{R}_c^{n_1}} + \frac{B}{\tilde{R}_c^{n_2}}, \quad (38)$$

where n_1 and n_2 are positive numbers, with n_1 being a small power in order to represent the dependence in extended envelopes.

The normalization of the temperature profile is regulated by \tilde{L} , since

$$T_{\text{ch}} \propto \tilde{L}^{-\frac{(k_\rho-1)}{2\beta+4(k_\rho-1)}} \quad (39)$$

from equation (7). This dependence is weak, but enables us to improve the accuracy of our fits - analogous to a temperature correction procedure. We may understand the variation of \tilde{L} with \tilde{R}_c as describing the transition from a modified blackbody to a protostellar envelope: In the limit of large optical depths, (small \tilde{R}_c) \tilde{L} is about 1 since most of the emission comes from the vicinity of a Rosseland photosphere. On the other hand, as \tilde{R}_c tends to infinity, the photosphere is less well-defined. In this limit, \tilde{L} is larger than unity, reflecting the effective increase in the total emitting area, as the intermediate frequencies probe the source function over the extended envelope. We depict the contribution functions for these two limiting cases in Figure 4. For large optical depths, \tilde{r}_m is approximately constant, since most of the emission comes from the surface and the photosphere is relatively well defined. On the other hand, at large \tilde{R}_c there is a wide range of r_m in the intermediate frequency regime. We find that this behavior can be represented by

$$\tilde{L} = A_L \tilde{R}_c^a, \quad (40)$$

with sufficient accuracy.

To determine the values of k_T , \tilde{L} , and C for given values of \tilde{R}_c and k_ρ , we use the downhill simplex method of Nelder and Mead (1965) to minimize the largest error between the shape of the normalized analytic spectrum and the normalized DUSTY spectrum. We ran DUSTY at an

intermediate value of L/M ($= 40L_\odot/M_\odot$), for $k_\rho = 1.1, 1.5$, and 2 , increasing Σ until we reached $T_{\text{ch}} = 200\text{K}$. To avoid calibrating our functional forms of k_T , \tilde{L} , and C with respect to higher values of T_{ch} , we then moved down the $T_{\text{ch}} = 200\text{K}$ isotherm towards large \tilde{R}_c until we reached $\Sigma = 0.03$. Along this line of constant L/M and this isotherm, we have ensured that the input luminosity equals the emergent luminosity. This is not exactly true away from this trajectory due to the weak dependence of the parameters on T_{ch} that we have ignored.

The temperature profile is determined by k_T and \tilde{L} . Our results for the slope of the temperature profile are:

$$k_T = \frac{0.48k_\rho^{0.05}}{\tilde{R}_c^{0.02k_\rho^{1.09}}} + \frac{0.1k_\rho^{5.5}}{\tilde{R}_c^{0.7k_\rho^{1.9}}} . \quad (41)$$

Figure 5 depicts k_T as a function of \tilde{R}_c . For \tilde{L} we find that

$$\tilde{L} = 0.87\tilde{R}_c^{0.084} \quad (42)$$

is sufficiently accurate for all k_ρ .

We find that setting $C = \text{constant}$ for each value of k_ρ allows for sufficient accuracy (in fact, letting C vary as a function of \tilde{R}_c does not increase accuracy). Values of $C(k_\rho)$ are selected to give good agreement with the break frequency for large \tilde{R}_c envelopes. This gives $C = 1, 0.9$, and 0.5 for $k_\rho = 1.1, 1.5$ and 2 respectively. For other values of k_ρ in the range $1 \leq k_\rho \leq 2$, C can be found from

$$C = 0.27 + 1.3k_\rho - 0.6k_\rho^2. \quad (43)$$

A more detailed discussion of this factor and its determination from the spectrum itself, i.e., the break frequency, for extended envelopes is given in §8.

We conclude with a caveat on our temperature specification procedure. The near-IR flux depends sensitively on the temperature profile, and we cannot recover the near-IR flux accurately with a single power law for the temperature profile. For example, as shown in Figure 3, it is clear that the emission at $5\mu\text{m}$, where there is an opacity minimum, originates inside the characteristic radius. Our single power law underestimates the temperature, and therefore the emission, for regions well inwards of the photosphere. This problem could be remedied with a two-component power law for the temperature profile, but that is not necessary here since we are focusing on emission at longer than near-IR wavelengths.

7. The Analytic SED and Its Accuracy

For convenience, we collect the equations that we have derived for the far-IR SED of dusty sources: The mm to far-IR SED is given by:

$$L_\nu = 16\pi^2(k_\rho - 1)R_{\text{ch}}^2 \left(\frac{2h\nu_{\text{ch}}^3}{c^2} \right) \tilde{\kappa}_\nu \tilde{\nu}^3 \tilde{r}_m^{2-k_\rho} \Delta\tilde{r}_m \exp \left[-\frac{h\nu}{kT(\tilde{r}_m)} - \tau_\nu(\tilde{r}_m) \right] . \quad (44)$$

The characteristic emission radius, $\tilde{r}_m = \tilde{r}_m(\nu)$, is the location in the shell where most of the flux in a given frequency-band originates from, (the “m” is for maximum), and is given by:

$$\tilde{r}_m = \text{Min}(\tilde{r}_{m,\text{low-int}} + \tilde{r}_{m,\text{high}}, 1) , \quad (45)$$

where the total r_m is the sum of the high frequency r_m and the combined low-intermediate frequency r_m ,

$$\tilde{r}_{m,\text{high}} = \left[\frac{\tilde{\kappa}_\nu(k_\rho - 1)}{\tilde{\nu}k_T} \right]^{1/(k_T + k_\rho - 1)} , \quad (46)$$

$$\tilde{r}_{m,\text{low-int}} = \frac{\tilde{R}_c C^{1/k_T}}{\tilde{R}_c \tilde{\nu}^{1/k_T} + C^{1/k_T}} . \quad (47)$$

The shell thickness, $\Delta\tilde{r}_m$ is given by:

$$\Delta\tilde{r}_m = \left[\frac{\Gamma\zeta \exp\left(\tilde{\nu}\tilde{r}_{m,\text{low-int}}^{k_T}\right)}{(3 - k_\rho - k_T)\tilde{\nu}\Gamma\zeta\tilde{R}_c^{-(3-k_\rho-k_T)} + k_T\tilde{\nu}^{(3-k_\rho)/k_T}} \right] \frac{1}{\tilde{r}_{m,\text{low-int}}^{2-k_\rho}} + \frac{(2\pi/h_m'')^{1/2}}{1 + 2\tilde{\kappa}_\nu\left(\frac{k_\rho-1}{k_\rho+1}\right)(\tilde{r}_{m,\text{high}}^{1-k_\rho} - \tilde{r}_{m,\text{high}}^2\tilde{R}_c^{-k_\rho-1})} , \quad (48)$$

where the argument $(3 - k_\rho)/k_T$ for the Gamma and Zeta functions has been suppressed for clarity, and h_m'' is given by Eqn. 30. The ratio of $h\nu$ to kT equals C for the intermediate frequencies and is given by:

$$C = 0.26 + 1.3k_\rho - 0.6k_\rho^2 \quad (49)$$

and

$$k_T = \frac{0.48k_\rho^{0.05}}{\tilde{R}_c^{0.02k_\rho^{1.09}}} + \frac{0.1k_\rho^{5.5}}{\tilde{R}_c^{0.7k_\rho^{1.9}}} . \quad (50)$$

The SED variables and the source parameters are related by:

$$\tilde{R}_c = \left\{ \frac{(L/M)\Sigma^{\frac{4+\beta}{\beta}}}{4\sigma \times 0.87} \left[\frac{(3 - k_\rho)\kappa_{\nu_0}}{4(k_\rho - 1)T_0^\beta} \right]^{4/\beta} \right\}^{-\frac{\beta}{1.92\beta + 4(k_\rho - 1)}} , \quad (51)$$

$$T_{\text{ch}} = \left\{ \frac{L/M}{4\sigma \times 0.87\Sigma^{\frac{2.92-k_\rho}{k_\rho-1}}} \left[\frac{4(k_\rho - 1)T_0^\beta}{(3 - k_\rho)\kappa_{\nu_0}} \right]^{\frac{1.92}{k_\rho-1}} \right\}^{\frac{k_\rho-1}{4(k_\rho-1)+1.92\beta}} , \quad (52)$$

where we have substituted for the values of A_L and a from (42).

The physical parameter space in which we have determined the accuracy of our analytic SED, as compared with the numerical solutions from DUSTY, is given in Figures 1, 6, and 7 for three density profiles, $k_\rho = 1.1, 1.5$ and 2. The parameter space extends over luminosity-to-mass ratios $L/M = (0.1 - 4000)L_\odot/M_\odot$ and surface densities $\Sigma = 0.01 - 100 \text{ g cm}^{-2}$, which encompass the full

range of astronomical dusty sources. We restrict our attention to $T_{\text{ch}} < 300$ K (250 K for $k_\rho = 1.1$) so that most of the emission is longwards of $30 \mu\text{m}$ and the slope of the temperature profile is approximately independent of T_{ch} . We also restrict our attention to $\tilde{R}_c > 1$, since our assumption of a spherical cloud with a sharp boundary is likely to break down for smaller envelopes. Within these boundaries, the SED given by the above equations is accurate to within a factor 2 at worst. The largest errors occur for $k_\rho = 1.1$; for $k_\rho = 1.5$, the SED is accurate to within a factor of 1.6, and for $k_\rho = 2$ it is accurate to within a factor 1.5. If we focus on surface densities in the range $0.01 - 3 \text{ g cm}^{-2}$, which is indeed where the majority of astrophysical sources lie, the accuracy is 1.5 for $k_\rho = 1.5$ and 1.3 for $k_\rho = 2$. We also note that our equations hold for $k_\rho = 1$, as numerical runs verify that $k_\rho = 1$ envelopes are well approximated by $k_\rho = 1.1$ (to better than 10 %) over our parameter space. Finally, we note that our largest errors, as compared to the numerical results, are at $30 \mu\text{m}$, on the low \tilde{R}_c end (large Σ region), where there is very little flux. As a result, our accuracy in inferring source parameters (given that our assumptions stated in §2 are satisfied) is generally better than a factor of 1.5, a point that we discuss in more detail in Paper II. SED fits, to a low-mass protostar, massive protostar, and ULIRG, respectively, are given in Figure 2a, Figure 2b, and Figure 2c.

We note here briefly (see Paper II for a more detailed explanation of the application of our methodology to observed data) that our accuracy criteria hold only so long as our assumptions are valid. In particular, many of the sources we consider in Paper II have significant high frequency fluxes that our solution cannot account for. High frequency emission can escape due to inhomogeneities in the envelope, due to the presence of an accretion disk, or from distributed sources of luminosity in the field of view that are not obscured by dust. We consider the effects of an inhomogeneous dust distribution in Paper III, and the effects of distributed sources of luminosity in Paper IV. To avoid fitting to data that may predominantly arise from one of these additional agents, in Paper II we have performed our fits from mm - $60 \mu\text{m}$, where these additional complexities are unlikely to significantly change the emitted spectrum. If the fit based on the mm - $60 \mu\text{m}$ data also fits the high frequency data, that is a good indication that the high frequency data are not due to these additional agents.

Our basic assumption of spherical symmetry can be violated by the presence of a disk that is large and massive enough to influence the far-IR spectrum. Since the disk radius approximately demarcates the region where the density, and therefore the temperature, profiles become nonspherical, our method is applicable only to the case in which the disk radius is smaller than the characteristic radius, $R_d < R_{\text{ch}}$. Even if this geometric condition is satisfied, we also require that emission at long wavelengths (where the emissivity scales as the product of the mass times the temperature) from the disk be small compared to that from the envelope, which implies

$$M_{\text{disk}} \ll M_{\text{env}} \left(\frac{T_{\text{env}}}{T_{\text{disk}}} \right). \quad (53)$$

We have also assumed that emission from the vicinity of the dust destruction radius at R_{dd} does not significantly influence the far-IR spectrum. A sufficient condition to ensure this is that the

optical depth to the dust destruction front at photospheric frequencies be large; we require $\tau > 3$ at the frequency ν_{peak} at which νL_ν peaks, which implies

$$\frac{R_{\text{dd}}}{R_c} < \frac{1}{\left(1 + 3\tilde{\nu}_{\text{peak}}^{-p} \tilde{R}_c^{k_\rho-1}\right)^{\frac{1}{k_\rho-1}}} . \quad (54)$$

Figure 8 depicts $\tilde{\nu}_{\text{peak}} = \nu_{\text{peak}}/\nu_{\text{ch}}$ as a function of \tilde{R}_c , and §8 gives corresponding fits to the curves. This optical depth condition is satisfied for $k_\rho = 2$ and $3/2$ for all \tilde{R}_c in our parameter space. It is also satisfied for $k_\rho = 1.1$ when $\tilde{R}_c \lesssim 10$. However, for $k_\rho = 1.1$ and $\tilde{R}_c \gtrsim 10$, the optical depth to the dust destruction front at ν_{peak} is not large. Nevertheless, emission from R_{dd} does not influence the spectrum because the far-IR luminosity originating from the vicinity of the dust destruction radius is small compared to that from the vicinity of the characteristic radius in our parameter space. An upper limit on emission from the vicinity of the dust destruction front is a blackbody radiating at T_{dd} . Hence, at intermediate frequencies, a sufficient condition for ignoring emission from the dust destruction front is

$$T_{\text{dd}} R_{\text{dd}}^2 \ll T_{\text{ch}} R_{\text{ch}}^2 \exp(-C) , \quad (55)$$

(with $h\nu/kT = C$), which is always satisfied in our parameter space. At frequencies well above ν_{peak} , where the emission from the vicinity of the dust destruction front is significant, the optical depth is large enough to suppress it.

8. Shape of SED: \tilde{R}_c and T_{ch}

As long as the assumptions stated in §2 & §7 are satisfied, i.e., given a spherically symmetric, homogeneous distribution of dust illuminated by a central source of radiation, such that the emitted spectrum is not significantly affected by emission from the dust destruction front, the shape of the long-wavelength SED will depend only on \tilde{R}_c for a given density profile and dust model. Thus, moving along a line of constant \tilde{R}_c preserves the shape of the SED, while shifting the peak of the SED as one intersects lines of different T_{ch} . The ratio of the peak frequency to the characteristic frequency is shown in Figure 8 and can be approximated as

$$\frac{\nu_{\text{peak}}}{\nu_{\text{ch}}} \simeq 0.82k_\rho + \frac{5.4 - 1.8k_\rho}{\tilde{R}_c^{0.56k_\rho - 0.22}} . \quad (56)$$

Similarly, moving along an isotherm, i.e., a line of constant T_{ch} , changes the shape of the SED as \tilde{R}_c changes but preserves near constancy of the peak of the SED since the variation of ν_{peak} with \tilde{R}_c is weak over most of the parameter space (see eq. 56).

Note that the ratio of the peak frequency to the characteristic frequency decreases as \tilde{R}_c increases because the intermediate frequencies, which are emitted at lower temperatures, become relatively more important in the total energy balance. In the low \tilde{R}_c regime (large optical depths),

our results are qualitatively similar to the blackbody limit, as $\nu_{\text{peak}} \sim 4\nu_{\text{ch}}$ (recall that ν_{peak} is the frequency at which νL_ν peaks). Over much of the astrophysical parameter space, however, spectra peak at $\nu_{\text{peak}} \sim (1 - 1.6)\nu_{\text{ch}}$.

Low mass protostars, as shown in Figure 9a, are characterized by large \tilde{R}_c and have broad SEDs. They have extended envelopes with temperatures low enough such that the intermediate frequency region, with its flatter slope, shows a clean separation from the low-frequency region. On the other hand, the far-IR spectra of massive protostars, ULIRGs and super-star clusters resemble quasi-blackbody spectra, where the low, intermediate, and high-frequency components have become smeared together (Figure 9b). Fits to observed data (Figure 2a, Figure 2b, and 2c) also display this variation of shape, as \tilde{R}_c varies over the parameter space, from the low-mass protostars to the massive protostars.

We also give the general relation between the characteristic parameters and the photospheric parameters. As noted earlier, our definition of the characteristic parameters coincides with photospheric parameters when core radius is much larger than R_{ch} . However, as \tilde{R}_c becomes small, the Rosseland photosphere moves to the surface of the core. Therefore, we approximate the relation between the photospheric and characteristic parameters as a harmonic mean of R_c and R_{ch} :

$$R_{\text{ph}} = \frac{R_{\text{ch}}}{1 + \tilde{R}_c^{-1}}. \quad (57)$$

We use $L = 4\pi R_{\text{ph}}^2 \sigma T_{\text{ph}}^4 = 4\pi R_{\text{ch}}^2 \sigma T_{\text{ch}}^4 \tilde{L}$ to see that the photospheric temperature varies as:

$$T_{\text{ph}} = T_{\text{ch}} \tilde{L}^{1/4} (1 + \tilde{R}_c^{-1})^{1/2}. \quad (58)$$

8.1. The Three-Component Spectrum of Extended Envelopes

We now consider the limiting case of highly extended envelopes, i.e., $\tilde{R}_c \rightarrow \infty$. We reach this region of astrophysical parameter space by moving downward and to the left along an isotherm towards low L/M and low Σ , i.e., past low mass protostars towards very low luminosity cores, or nearly prestellar cores. Figure 11 depicts a large \tilde{R}_c envelope and its corresponding contribution function, with the break frequency marked in both diagrams. We note that in this limiting case, since $k_T \rightarrow \text{constant}$, we may infer the source parameters from ν_{peak} and ν_{break} only. The peak frequency is given by equation 56; the break frequency is given in terms of L/M and Σ by

$$\tilde{\nu}_{\text{break}} = C \left\{ \frac{(L/M)\Sigma^{(4+\beta)/\beta}}{4\sigma 0.87} \left[\frac{(3 - k_\rho)\kappa_{\nu_0}}{4(k_\rho - 1)T_0^\beta} \right]^{4/\beta} \right\}^{\beta k_T / [1.92\beta + 4(k_\rho - 1)]}. \quad (59)$$

where C is given in equation 43. Figure 10 depicts the factor $C(\tilde{R}_c)$ for the three standard density profiles; as shown, $C \rightarrow \text{constant}$ for large \tilde{R}_c .

The clean separation of the intermediate frequency regime in this limiting case allows us to specify the temperature dependence of the spectrum in the intermediate frequency regime,

$$L_\nu \propto T_{\text{ch}}^{7-3k_\rho}, \quad (60)$$

which follows from Eqn. 12 and Eqn. 17 with $k_T = 1/3$ and $\beta = 2$. The slope of $k_\rho = 1.1, 1.5$ and 2 envelopes depends on T_{ch}^4 , $T_{\text{ch}}^{5/2}$, and T_{ch} respectively, so that $k_\rho = 1.1$ envelopes are most sensitive to the temperature.

As we discuss in §8.3, while it is not generally feasible to discriminate density profiles from the far-IR spectra of unresolved sources, it is possible to do so for extended envelopes. In this case, we may write down a simple expression for the intermediate frequency slope, which holds for $1 \gtrsim \tilde{\nu} \gtrsim \tilde{\nu}_{\text{break}}$:

$$L_\nu \propto \nu^{3+\beta-(3-k_\rho)/k_T(\tilde{R}_c)}. \quad (61)$$

For envelopes that are sufficiently extended ($\tilde{R}_c \gtrsim 2000$), one can infer k_ρ directly from the measured slope in the intermediate frequency regime. The pristine environments of isolated, low-luminosity cores allow for the most robust determination of the density profile from the far-IR SED, without requiring resolved observations of the source itself. Such a determination of the density profiles for these sources would also provide a direct observational test of the star formation scenario, as different theories of star formation are characterized by different density profiles.

8.2. Density Profile

The inference of density profiles from the far-IR SED has been treated in various ways in the literature. Some authors have determined the density profile from fitting to the SED and the intensity profile concomitantly (Shirley et al 2002, Mueller et al 2002, Beuther et al 2002), which works if the intensity is solved for self-consistently. The Adams (1991) approximation for the spatial distribution of the millimeter and submillimeter emission, and its use to infer density profiles (e.g. Beuther et al 2002), is based on the assumption that $1/3 \lesssim k_T \lesssim 2/5$, which is a good approximation for large \tilde{R}_c . However, the dense envelopes of massive protostars imply they are characterized by lower values of \tilde{R}_c , and therefore higher values of k_T . Hence, the accuracy of the Adams approximation for dense envelopes is degraded in this region of the parameter space. Some authors (e.g. van der Tak et al 2000, OLD99) have claimed that density profiles can be inferred from the observed SED alone. Others, (e.g. Correia et al 2004) have noted that varying density profiles give equally good fits to the SED. Therefore, the question remains: under what conditions can the density profile be inferred from the mm to far-IR SED alone?

So far, we have shown that for a given density profile and dust model, the SED is a function only of L/M and Σ . To address the question of whether inference of density profiles is feasible, we now ask under what conditions can one distinguish the predicted mm to far-IR fluxes for envelopes characterized by different density profiles? To do this, we consider SEDs produced by envelopes

characterized by the same L/M and Σ , but with different density profiles. Figure 12a depicts the the 1mm to 60 μ m flux ratio vs. the the 30 μ m to 60 μ m flux ratio for the three density profiles, $k_\rho = 1.1, 3/2, 2$, with each trio having the same L/M and Σ values. The $k_\rho = 3/2$ points (crosses) correspond to an isotherm, $T_{\text{ch}} = 210$ K, with the bottommost point corresponding to $\tilde{R}_c = 43$ and the topmost point to $\tilde{R}_c = 370$. Note that for the first two trios, the colors for the different density profiles are not clearly distinguishable (i.e., they do not differ by more than a factor of two), while for the third trio ($\tilde{R}_c = 180, T_{\text{ch}} = 210$ K for $k_\rho = 3/2$) they are. Thus, the different density profiles are distinguishable at sufficiently large \tilde{R}_c . The region in the $L/M - \Sigma$ plane in which at least one of the two colors differs by at least a factor 2 between the $k_\rho = 1.1$ and $k_\rho = 2$ cases is shown in Figure 12b.

The basic intuition behind this result is that envelopes with large values of \tilde{R}_c (i.e., envelopes in which the photosphere is small compared to the size of the core) have an extended range of intermediate frequency emission in the far-IR. Emission at intermediate frequencies originates from a range of radii and temperatures, and as a result, the emission from large \tilde{R}_c envelopes depends more sensitively on the density profile than that from low or moderate \tilde{R}_c envelopes. This is true for any value of T_{ch} , i.e., it will be easier to discriminate density profiles for larger values of \tilde{R}_c whether we consider sources at high T_{ch} or low T_{ch} . However, as shown in Figure 12b, there is some dependence on T_{ch} , since the ratio of the 30 μ m emission to 60 μ m emission is sensitive to the temperature; this effect is ameliorated by the fact $\nu_{\text{peak}}/\nu_{\text{ch}}$ increases at low values of \tilde{R}_c , where T_{ch} is low also.

We conclude that while it may be feasible to infer the density profile from the SED for low and intermediate mass protostellar sources, it is difficult to do so for high-mass protostars and extragalactic sources as they are generally on the low \tilde{R}_c end of the parameter space.

9. Conclusion

We have presented an analytic, self-consistent solution for the spectral energy distribution of homogenous, spherically symmetric, dust-enshrouded central sources of radiation that are not affected by emission from the dust destruction radius. The main points are:

1. For a given dust model and density profile, the SED is determined by three parameters, the luminosity of the central source, L , the mass of the envelope, M , and the size of the envelope, R_c . The *shape* of the SED is distance independent, and is determined by the two distance-independent parameters L/M and $\Sigma \equiv M/(\pi R^2)$. The cases of greatest relevance in astrophysics have $0.1L_\odot/M_\odot \lesssim L/M \lesssim 4000L_\odot/M_\odot$ and $0.01 \text{ g cm}^{-3} \lesssim \Sigma \lesssim 100 \text{ g cm}^{-3}$. We consider power-law density profiles, $\rho \propto r^{-k_\rho}$, with $1 \leq k_\rho \leq 2$.

2. The characteristic radius, R_{ch} , is analogous to a Rosseland photosphere. The characteristic temperature, T_{ch} , is given by $L = 4\pi\tilde{L}R_{\text{ch}}^2\sigma T_{\text{ch}}^4$, where \tilde{L} is a number of order unity. The emission at a frequency ν can be viewed as originating from a shell centered at $r_m(\nu)$, with thickness $\Delta r_m(\nu)$

and with an attenuation $e^{-\tau(\nu)}$. Most of the emission originates outside R_{ch} , since for $h\nu \gtrsim kT_{\text{ch}}$ the optical depth is large, whereas for $h\nu \lesssim kT_{\text{ch}}$ most of the emitting mass is outside the photosphere.

3. The SED is readily described in terms of the characteristic temperature, T_{ch} , and the dimensionless parameter $\tilde{R}_c \equiv R_c/R_{\text{ch}}$. For a given dust model and density profile, T_{ch} and \tilde{R}_c are unique functions of L/M and Σ . Low-mass protostars have extended envelopes with core radii that are large compared to the photospheric radius, so that $\tilde{R}_c \gg 1$. High-mass protostars, ULIRGs and super-star clusters generally have less extended envelopes (smaller values of \tilde{R}_c). The width of the SED correlates with \tilde{R}_c : sources with small values of \tilde{R}_c have quasi-blackbody SEDs, whereas those with large values of \tilde{R}_c have broad SEDs.

4. The SED has three frequency regimes. Low frequencies are emitted by the entire envelope, and have $h\nu < kT(R_c)$. For the density profiles we have considered, most of the low-frequency emission comes from the outer part of the envelope; it is optically thin. Intermediate frequencies have $kT(R_c) < h\nu \lesssim kT_{\text{ch}}$, so that they are suppressed in the outer envelope; most of the emission is optically thin. Finally, high frequencies have $h\nu \gtrsim kT_{\text{ch}}$. The flux at high frequencies is the result of a competition between the opacity, which favors emission from larger radii, and the temperature, which favors emission from smaller radii, where the dust is warmer. Low frequencies vary as $\nu^{2+\beta}$, intermediate frequencies vary as $\nu^{3+\beta-(3-k_\rho)/k_T(\tilde{R}_c)}$, and high frequencies have a “super-Wien” behavior - they fall off faster than $\nu^3 \exp(-h\nu/kT)$.

5. We approximated the temperature profile near the photosphere as a power law, $T \propto r^{-k_T}$, where the temperature gradient, k_T , is determined from imposing the self-consistency condition that the input luminosity exactly equal the emergent luminosity. We then showed that adoption of this approximate temperature profile leads to good agreement (usually within a factor ~ 1.5 between 3 mm and 30 μm) with spectra calculated with the numerical radiative transfer code DUSTY.

6. Longwards of 30 μm , where the opacity is scale free, the shape of the SED is a function only of \tilde{R}_c and k_ρ . However, the dependence on the density profile (k_ρ) is significant only for relatively large values of \tilde{R}_c . Large \tilde{R}_c envelopes, such as those of low-luminosity, low-mass protostars, present an opportunity to infer the source parameters from two observable frequencies, ν_{peak} and ν_{break} , where ν_{break} divides the low and intermediate frequency regimes. At large \tilde{R}_c , the intermediate frequency regime has a slope that depends explicitly on k_ρ .

We thank Bruce Draine, Eugene Chiang, David Hollenbach, Xander Tielens, and especially Gibor Basri for helpful discussions. We also thank Maia Nenkova and Dejan Vinkovic for answering innumerable DUSTY-related questions. This research is supported in part by NSF grant AST00-98365. CFM gratefully acknowledges the support of the Miller Foundation for Basic Research. SC gratefully acknowledges a dissertation year fellowship from the Graduate Opportunity Program.

A. Relation to DUSTY Parameters

We give the relations between the characteristic parameters and the DUSTY parameters. First, we note that the DUSTY dimensionless parameters are: $y = R_c/R_{\text{dd}} = \tilde{R}_c/\tilde{R}_{\text{dd}}$; τ_{ν_0} , the optical depth through the shell at frequency ν_0 ; and k_ρ , the slope of the density profile. The dimensional parameters are the dust destruction temperature, T_{dd} , and the temperature of the central illuminating source, T_* . In addition, the shape of the opacity curve is required as input. The dust destruction radius, R_{dd} , can be expressed as

$$R_{\text{dd}} = \left[(1 + 0.007\tau_V) \frac{\bar{Q}_{\text{UV}}}{\bar{Q}_{\text{IR}}} \frac{L}{16\pi\sigma T_{\text{dd}}^4} \right]^{1/2}, \quad (\text{A1})$$

as in IE97.

Thus, the value of the dust destruction radius depends explicitly on the magnitude of the luminosity. For our purposes, the parameters T_{dd} and R_{dd} do not enter into the problem, as we consider optical depths to the dust destruction radius large enough such that it is opaque at far-IR wavelengths. We choose ν_0 to be in the power-law portion of the opacity curve so that we may express τ_{ν_0} as

$$\tau_{\nu_0} = \left(\frac{h\nu_0}{kT_{\text{ch}}} \right)^\beta \left(\tilde{R}_{\text{dd}}^{-k_\rho+1} - \tilde{R}_c^{-k_\rho+1} \right), \quad (\text{A2})$$

where $\tilde{R}_{\text{dd}} \equiv R_{\text{dd}}/R_{\text{ch}}$.

B. Escape Fraction

Here, we give the derivation of the escape fraction for spherical geometry:

$$f(r) = \int_{\mu=0}^{\mu=1} e^{-\tau_\nu(r,\mu)} d\mu, \quad (\text{B1})$$

where $\mu = \cos(\theta)$. For escape at small angles (which is appropriate for large optical depth), we evaluate $\tau(\theta)$ for $\theta \ll 1$. We express the optical depth as:

$$\tau_\nu = \tilde{\kappa}_\nu(k_\rho - 1) \int r'^{-k_\rho} d\tilde{s}, \quad (\text{B2})$$

where the path length is equal to

$$ds = \frac{r' dr'}{[r^2 + r'^2(\mu^2 - 1)]^{1/2}}, \quad (\text{B3})$$

with r as the source point. We evaluate the optical depth for $\theta \ll 1$, to find that:

$$\tau_\nu(r, \theta) = \tau_\nu(r, 0) + \frac{\frac{1}{2}\theta^2 r^2 \tilde{\kappa}_\nu(k_\rho - 1)}{k_\rho + 1} (\tilde{r}^{1-k_\rho} - \tilde{r}^2 \tilde{R}_c^{-1-k_\rho}). \quad (\text{B4})$$

Now, we evaluate the integral for the escape fraction with respect to angle and find that:

$$f(r) = \frac{(k_\rho + 1)e^{-\tau_\nu(r,0)}}{2\tilde{\kappa}_\nu(k_\rho - 1)(\tilde{r}^{1-k_\rho} - \tilde{r}^2\tilde{R}_c^{-1-k_\rho})}, \quad \tau_\nu(r,0) \gg 1. \quad (\text{B5})$$

We assume that the $\tau_\nu(r,0) = 1$ surface is at $r \ll R_c$, so that the escape fraction is unity near the surface of the core. We recover the proper limit when $r = R_c$, i.e., we recover $f = 1$ in that case, if we modify this to be:

$$f(r) = \frac{e^{-\tau_\nu(r,0)}}{1 + 2\tilde{\kappa}_\nu\left(\frac{k_\rho-1}{k_\rho+1}\right)\left(\tilde{r}^{1-k_\rho} - \tilde{r}^2\tilde{R}_c^{-k_\rho-1}\right)}. \quad (\text{B6})$$

REFERENCES

- Adams, F.C., 1991, ApJ, 382, 544
- Adams, F.C., Lada, C.J., & Shu, F.H., 1987, ApJ, 312, 788
- Adams, F.C. & Shu, F.H., 1985, ApJ, 296, 655
- Allamandola, L.J., Sandford, S.A., Tielens, A.G.G.M., & Herbst, T.M., 1992, ApJ, 399, 134A
- Andre, P., Ward-Thompson, D., & Barsony, M. 1993, ApJ, 406, 122
- Bergin, E.A., Lellouch, E., Harwit, M., et al 2000, ApJ, 539L, 147B
- Beuther, H., Schilke, P., Menten, K.M., Motte, F., Sridharan, T.K. & Wyrowski, F., 2002, ApJ, 566, 945
- Beuther, H., & Schilke, P., 2004, Science, 303, 1167B
- Blain, A.W., Smail, I., Ivison, R.J., Kneib, J.P. & Frayer, D.T., 2002, PhR, 369, 111
- Blitz, L., & Williams, J.P. 1997, ApJ, 488, L145
- Bonnell, I.A., Bate, M.R. & Zinnecker, H., 1998, MNRAS, 298, 93
- Calzetti, D., Armus, L., Bohlin, R.C., et al 2000, ApJ, 533, 682
- Cesaroni, R., Felli, M., et al 1999, A&A 345, 949C
- Chakrabarti, S., & McKee, C.F., Paper II
- Chakrabarti, S., & McKee, C.F., Paper III
- Chapman, S.C., Smail, I, et al 2004, ApJ, 614: 671
- Downes, D., & Solomon, P.M., 1998, ApJ, 507, 615
- Draine, B.T. & Lee, H.M., 1984, ApJ, 285, 89
- Dunne, L. & Eales, S.A., 2001, MNRAS, 327, 697
- Efstathiou, A. & Rowan-Robinson, M., 1991, MNRAS, 252, 528

- Fontani, F., Cesaroni, R., Testi, L et al, 2004, A&A, 414, 299F
- Genzel, R., & Cesarsky, C. 2000, ARAA, 38, 761
- Genzel, R., Lutz, D., Sturm, E., et al 1998, ApJ, 498, 579
- Genzel, R., Baker, A., et al, 2003, ApJ, 584, 633
- Gilbert, A.M. & Graham, J.R, 2001, BAAS, 199, 14.04
- Gilbert, A.M., 2002, Ph.D. Thesis, University of California, Berkeley, Source DAI-B 64/02, p. 762
- Hildebrand, R.H., 1983, QJRAS, 24, 267
- Ivezic, Z. & Elitzur, M., 1997, MNRAS, 287, 799
- Jorgensen, J.K., Schoier, F.L., & van Dishoeck, E.F., 2002, A&A, 389, 908
- Kandori, R., Dobashi, K., et al 2003, AJ, 126, 1888
- Lada, C.J. 1987, in Star Forming Regions, ISU Symp. 115, ed. M. Peimbert & J. Jugaku (Dordrecht: Reidel), p. 1
- Lada, C.J., & Wilking, B. 1984, ApJ, 287, 610
- Larson, R.B., 1969, MNRAS, 145, 297
- Li A. & Draine, B.T., 2001, ApJ, 554, 778
- Kenyon, S.J., Calvet, N. & Hartmann, L., 1993, ApJ, 414, 676
- McKee, C.F. & Tan, J.C., 2002, Nature, 416, 59
- McKee, C.F. & Tan, J.C., 2003, ApJ, 585, 850
- McLaughlin, D.E. & Pudritz, R.E., 1997, ApJ, 476, 750
- Mueller, K.E., Shirley, Y.L, Evans, N.J.II & Jacobsen, H.R., 2002, ApJS, 143, 469
- Nakano, T., Hasegawa, T., Morino, J., & Yamashita, T., 2000, ApJ, 534, 976
- Nenkova, M., Ivezic, Z. & Elitzur, M., 2002, ApJ, 570L, 9
- Ossenkopf, V. & Henning, Th., 1994, AJ, 291, 943
- Osorio, M., Lizano, S. & D’Alessio, P., 1999, ApJ, 525, 808
- Plume, R., Jaffe, D.T., Evans, N.J. II, Martin-Pintado, J., Gomez-Gonzalez, J., 1997, ApJ, 476, 730
- Pollack, J.B., Hollenbach, D., Beckwith, S., Simonelli, D.P., Roush, T. & Fong, W., 1994, ApJ, 421, 615
- Poppe, T., Blum, J., & Henning, T., 2000, ApJ, 533, 472
- Preibisch, Th., Zinnecker, H., & Schmitt, J.H.M.M., 1993, A&A, 279L, 33P
- Shirley, Y.L, Evans, N.J., & Rawlings, J.M.C., 2002, ApJ, 575, 337
- Soifer, T., et al. 1984, ApJ, 278, L71

- Soifer, B.T., et al. 2000, *AJ*, 119, 509S
- Spoon, H.W.W., Keane, J.V., Tielens, A.G.G.M., Lutz, D., Moorwood, A.F.M., & Laurent, O., 2002, *A&A*, 385, 1022S
- Strafella, F., Campeggio, L, et al 2001, *ApJ*, 558, 717
- Tielens, A.G.G.M., Allamandola, L.J., et al, 1984, *ApJ*, 287, 697T
- van der Tak, F.S., van Dishoeck, E.F., Evans, N.J. & Blake, G.A., 2000, *ApJ*, 537, 283
- Weingartner, J.C. & Draine, B.T., 2001, *ApJ*, 548, 296
- Whitney, B.A., Wood, K., Bjorkman, J.E., & Cohen, M., 2003, *ApJ*, 598, 1079
- Williams, J.P., Blitz, L, & McKee, C.F, 2000, *PPIV*, 97
- Wolfire, M.G. & Cassinelli, J.P., 1987, *ApJ*, 319, 850
- Wolfire, M.G. & Cassinelli, J.P., 1986, *ApJ*, 310, 207
- Wynn-Williams, C.G. & Becklin, E.E, 1993, *ApJ*, 412, 535
- Xu, C., Hacking, P.B., Fang, F., Shupe, D.L., Lonsdale, C.J., Lu, N.Y., Helou, G., Stacey, G.J., & Ashby, M., L.N., 1998, *ApJ*, 508, 579
- Xu, C., Lonsdale, C.J., Shupe, D.L., O’Linger, J., Masci, F., 2001, *ApJ*, 562, 179
- Yorke, H.W. & Sonnhalter, C., 2002, *ApJ*, 569, 846
- Yun, M.S. & Carilli, C.L., 2002, *ApJ*, 568, 88

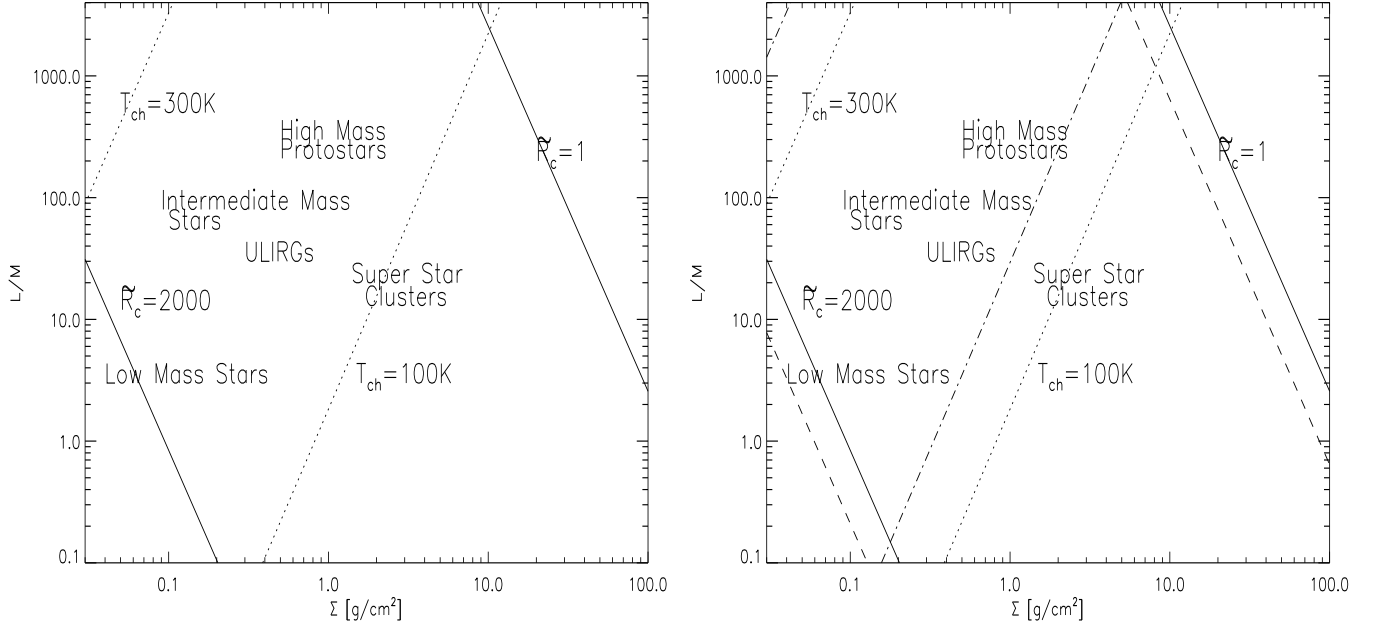


Fig. 1.— (a) $L/M[L_{\odot}/M_{\odot}]$ vs $\Sigma[\text{g}/\text{cm}^2]$ for fiducial density profile, $k_{\rho} = 3/2$. T_{ch} is the effective photospheric temperature and \tilde{R}_c is the ratio of the core radius to R_{ch} , which is like the Rosseland photosphere (b) with change in opacity normalization of a factor of two (dashed line), due to ice-mantles

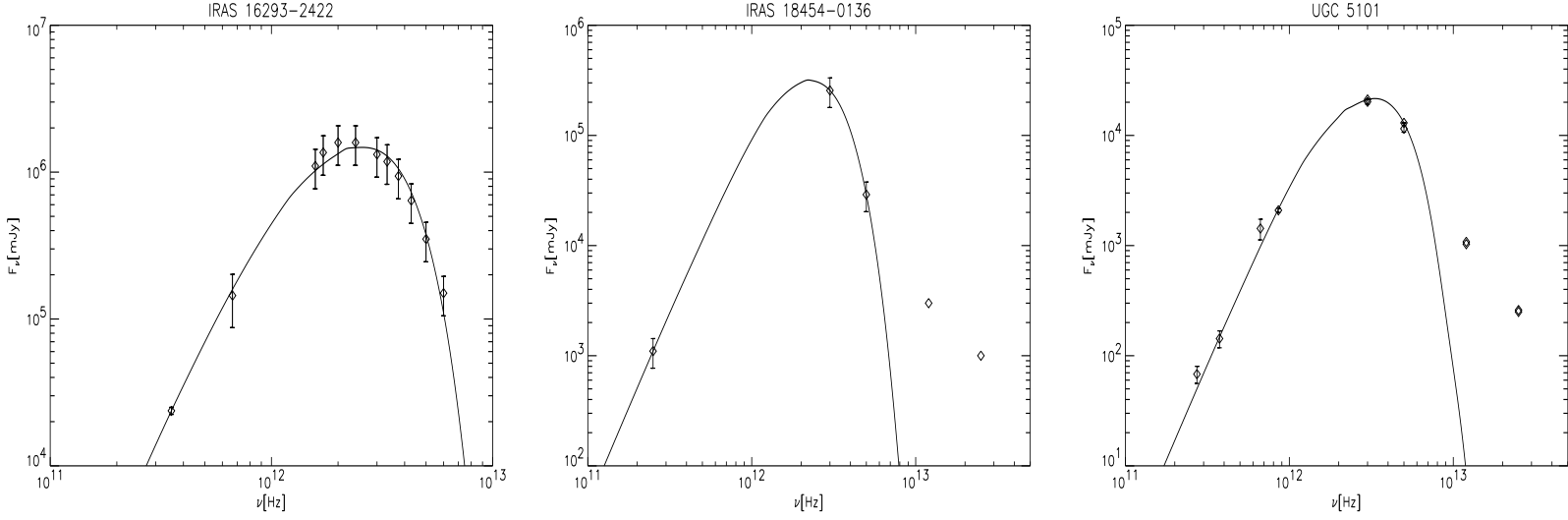


Fig. 2.— (a) SED fit to low-mass protostar, $L/M \sim 7L_\odot/M_\odot$, $\Sigma \sim 0.3\text{g cm}^{-2}$ (b) SED fit to massive protostar, $L/M \sim 11L_\odot/M_\odot$, $\Sigma \sim 1.5\text{g cm}^{-2}$, (c) SED fit to ULIRG, $L/M \sim 33L_\odot/M_\odot$, $\Sigma \sim 0.3\text{g cm}^{-2}$. Details of fitting procedure and inferred parameters given in Paper II

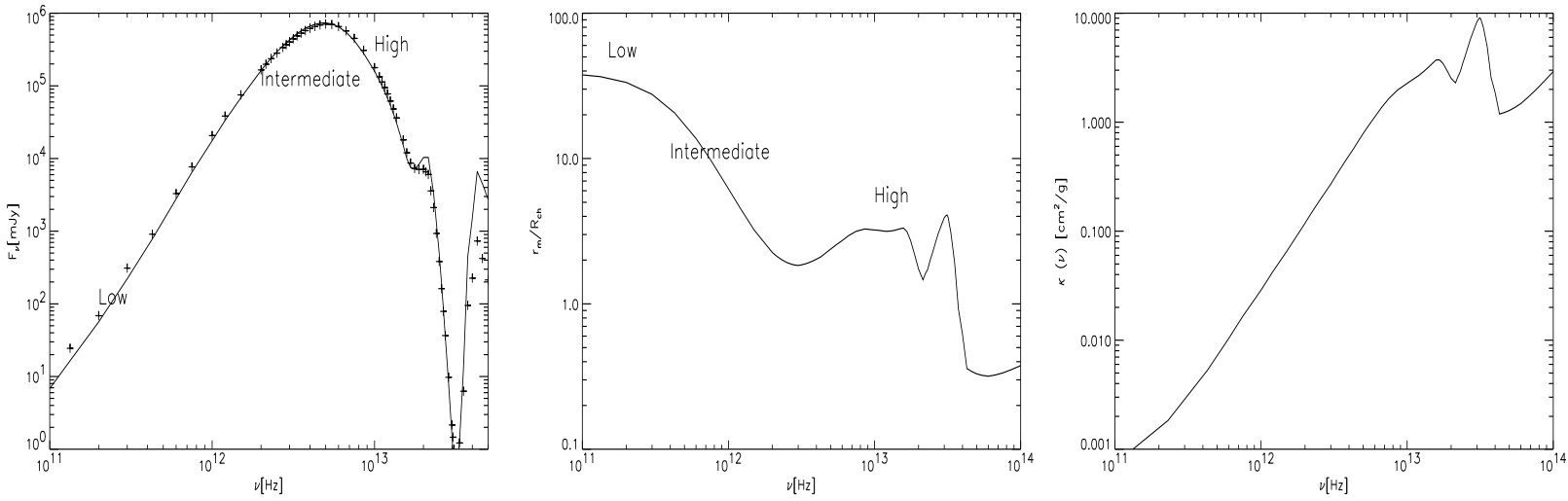


Fig. 3.— (a) SED for typical high mass protostar with frequency regimes marked (solid line is DUSTY SED and crosses analytic SED) (b) Contribution function (the characteristic emission radius), in dimensionless units, \tilde{r}_m , with frequency regimes marked, (c) WD01 opacity curve. The spectral features in the SED and opacity curve as shown in (a) and (c), e.g. the 3×10^{13} Hz ($10\mu\text{m}$) absorption feature, correlate with the location in the envelope this emission is coming from, as shown in (b)

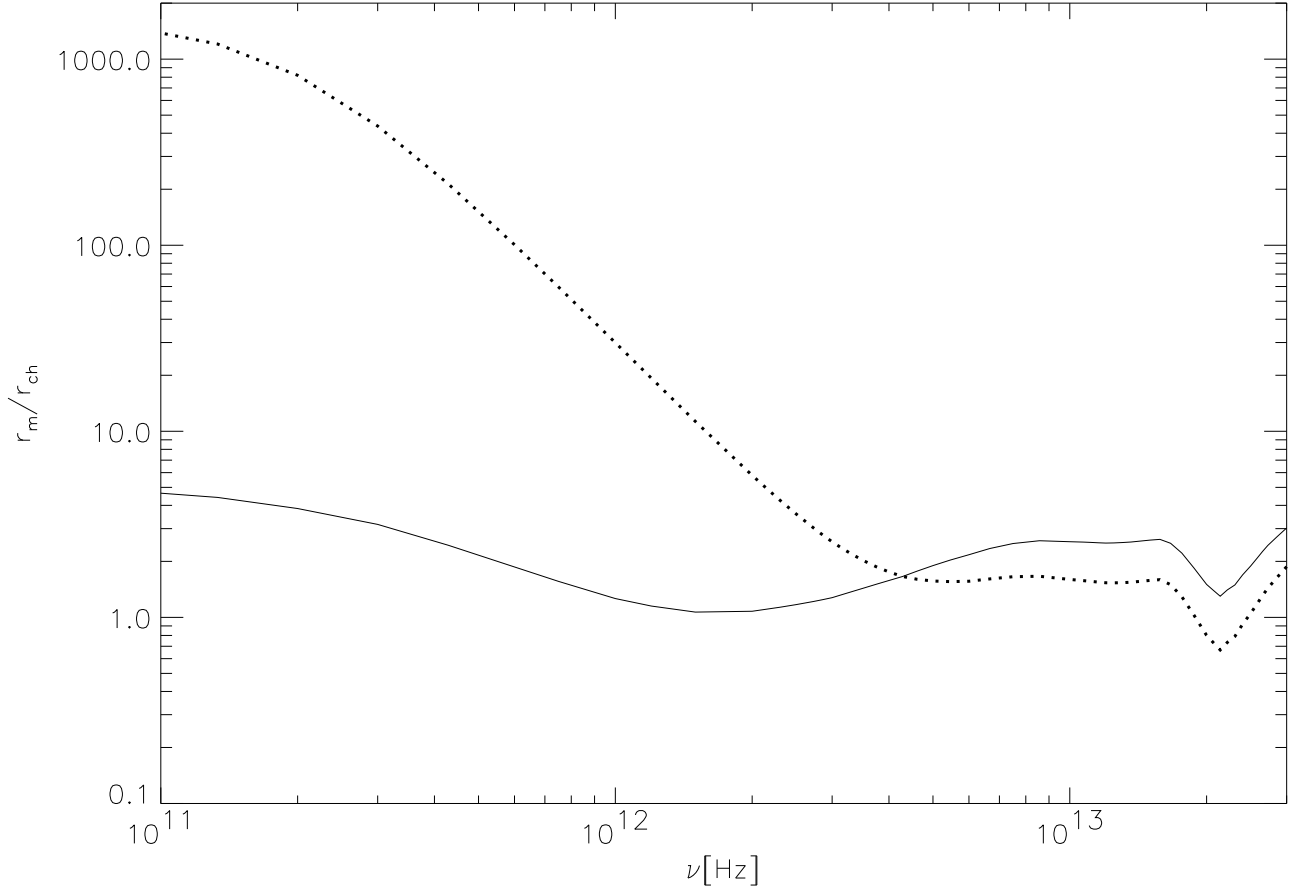


Fig. 4.— Contribution function (the characteristic emission radius), in dimensionless units, \tilde{r}_m , for a compact envelope, $\tilde{R}_c = 4$ (solid line), and for an extended envelope, $\tilde{R}_c = 2000$ (dotted line)

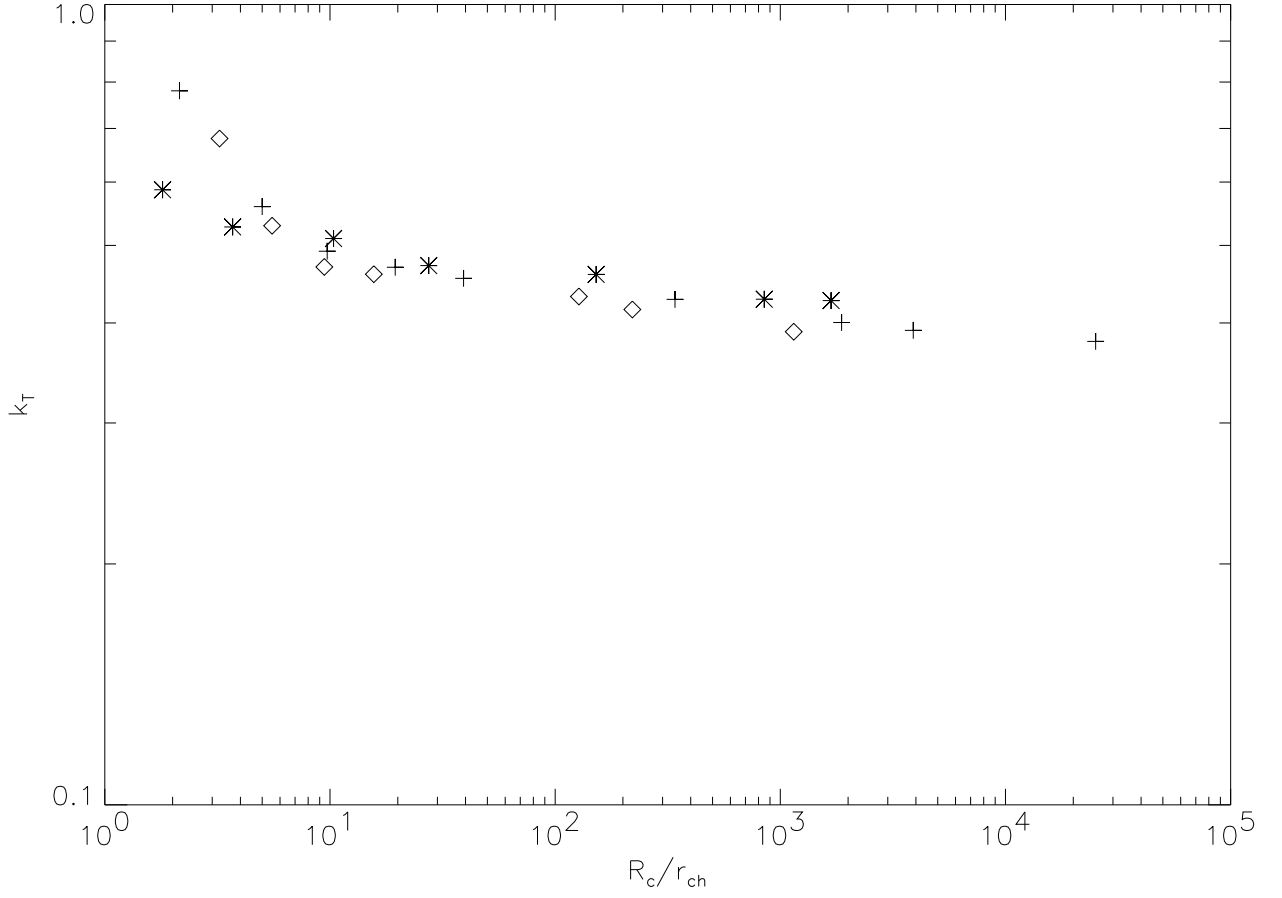


Fig. 5.— (a) Slope of temperature profile, k_T as a function of \tilde{R}_c . Asterisks denote $k_\rho = 1$, crosses denote $k_\rho = 3/2$, and diamonds denote $k_\rho = 2$

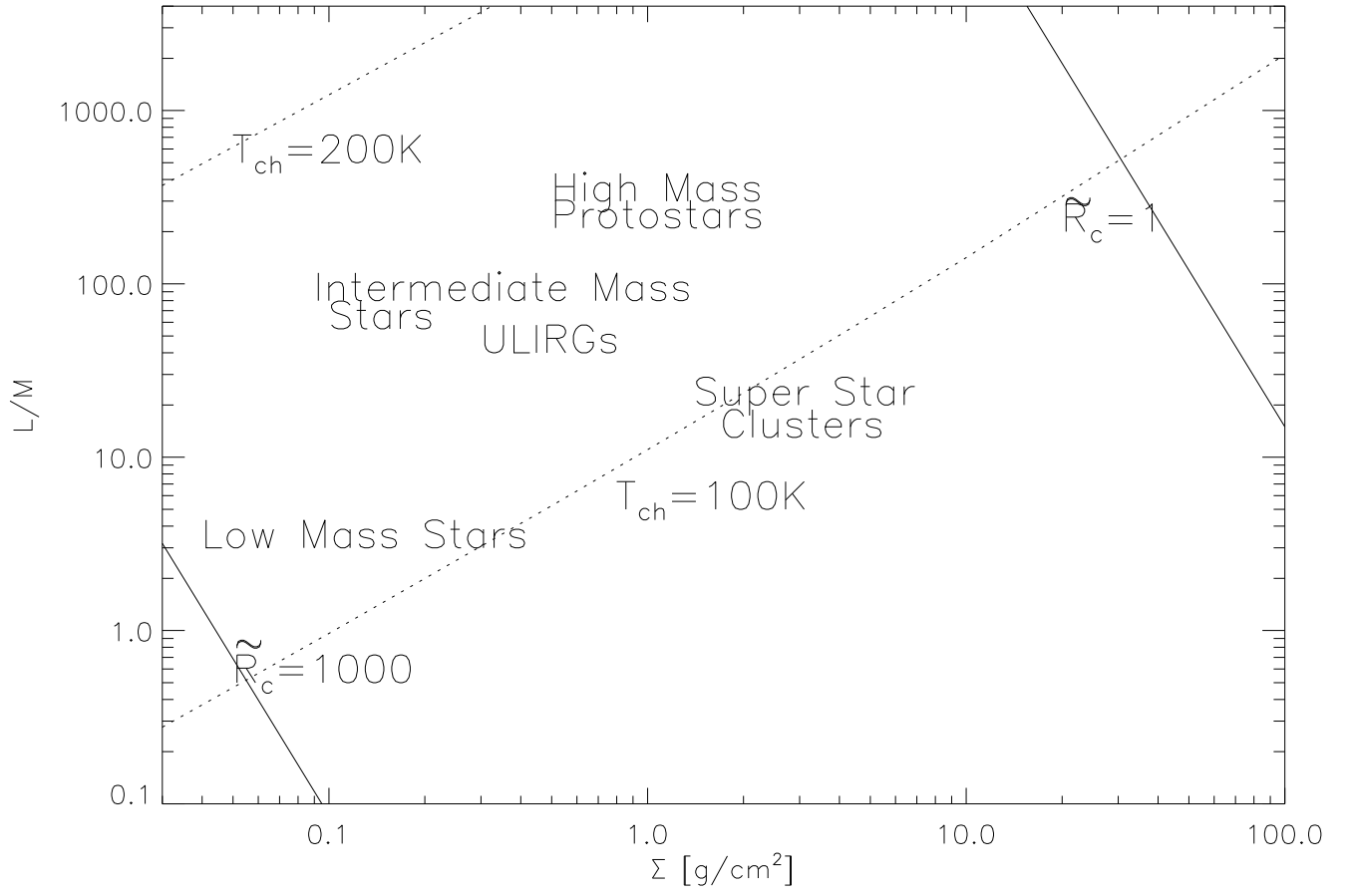


Fig. 6.— $L/M[L_\odot/M_\odot]$ vs $\Sigma[\text{g/cm}^2]$ for $k_\rho = 2$

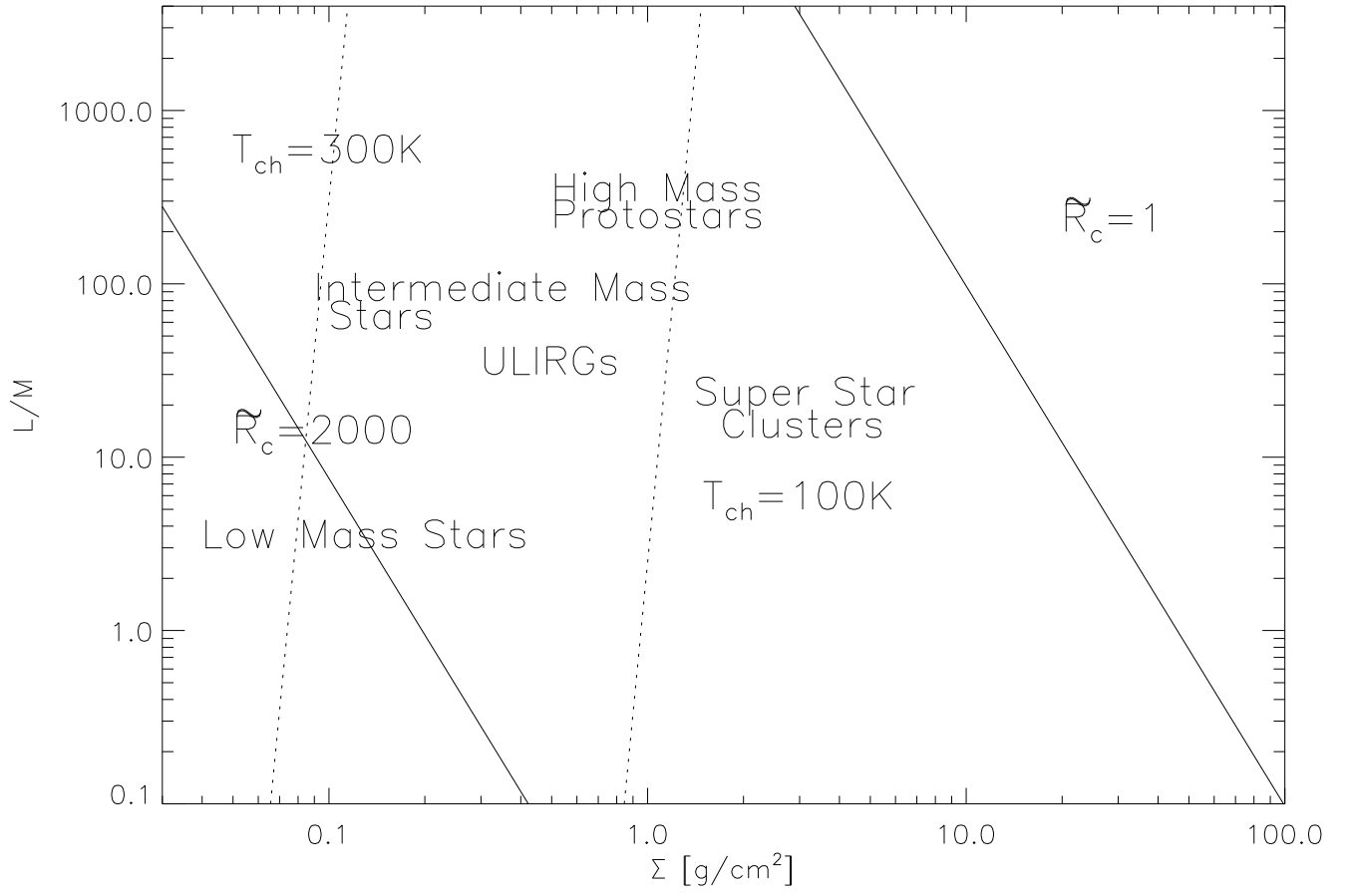


Fig. 7.— $L/M[L_{\odot}/M_{\odot}]$ vs $\Sigma[\text{g}/\text{cm}^2]$ for $k_{\rho} = 1$

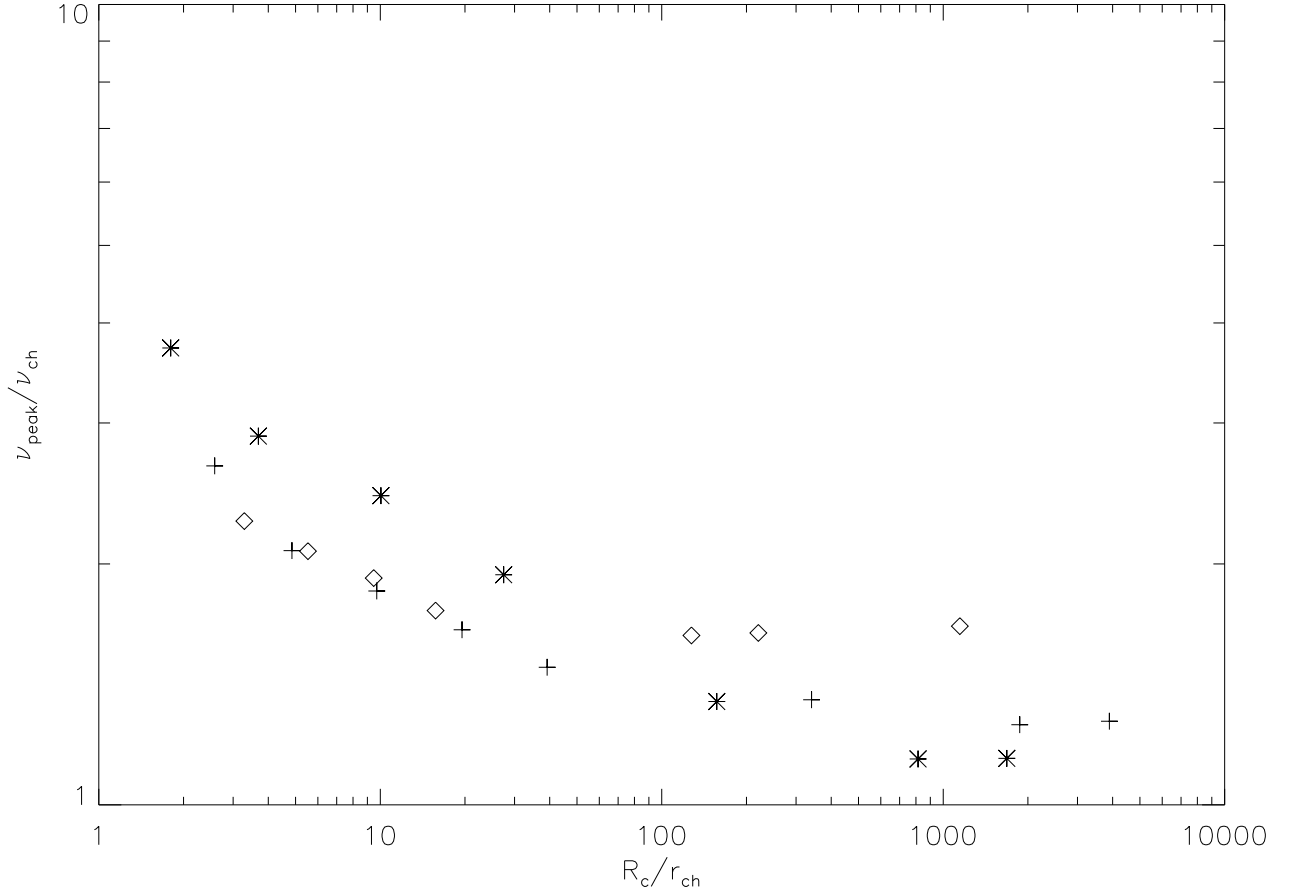


Fig. 8.— The ratio of the peak frequency to the characteristic frequency, ν_{peak}/ν_{ch} , as a function of \tilde{R}_c . Asterisks denote $k_\rho = 1$, crosses denote $k_\rho = 3/2$, and diamonds denote $k_\rho = 2$.

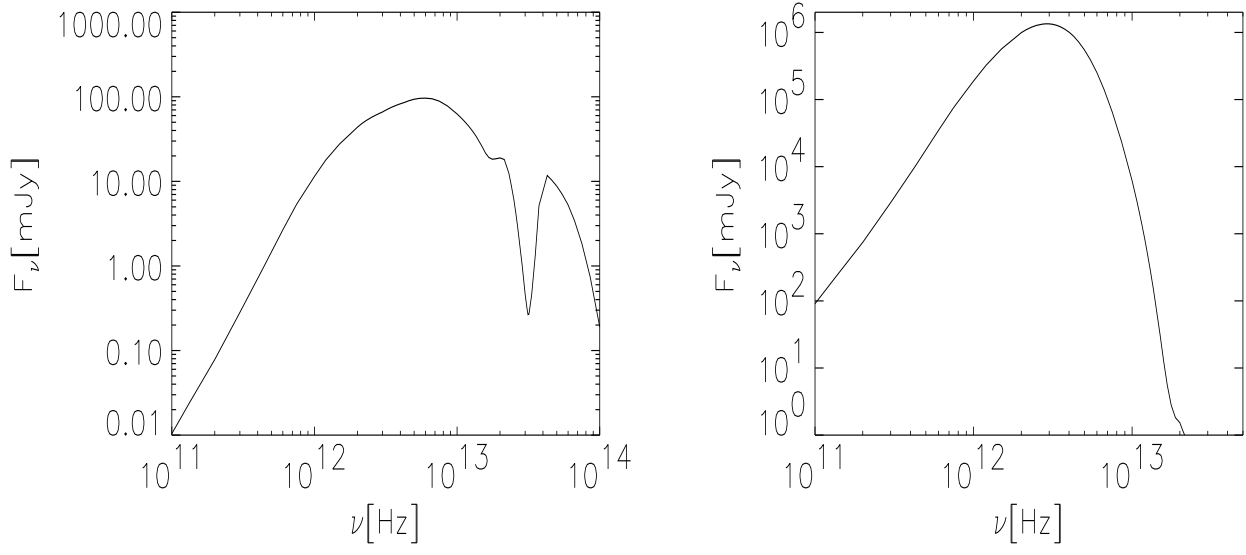


Fig. 9.— (a) Far-IR SED for typical low mass protostar, (b) Far-IR SED of typical ULIRG

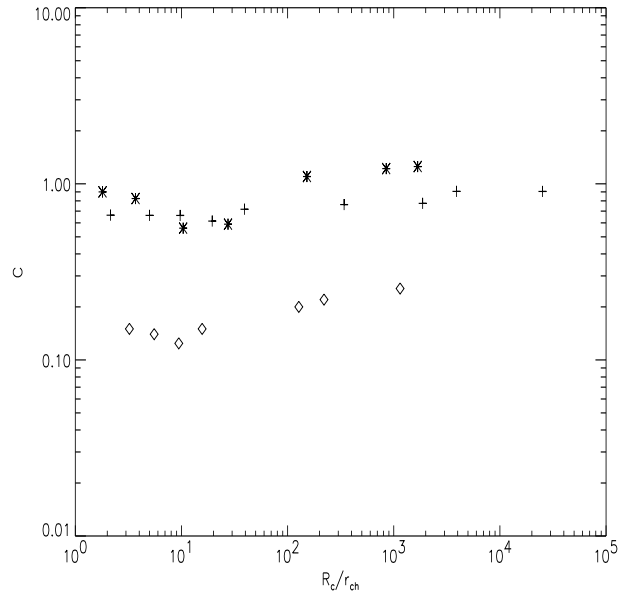


Fig. 10.— $C(\tilde{R}_c)$ for $k_\rho = 3/2$ (crosses), $k_\rho = 1$ (asterisks), and $k_\rho = 2$ (diamonds)

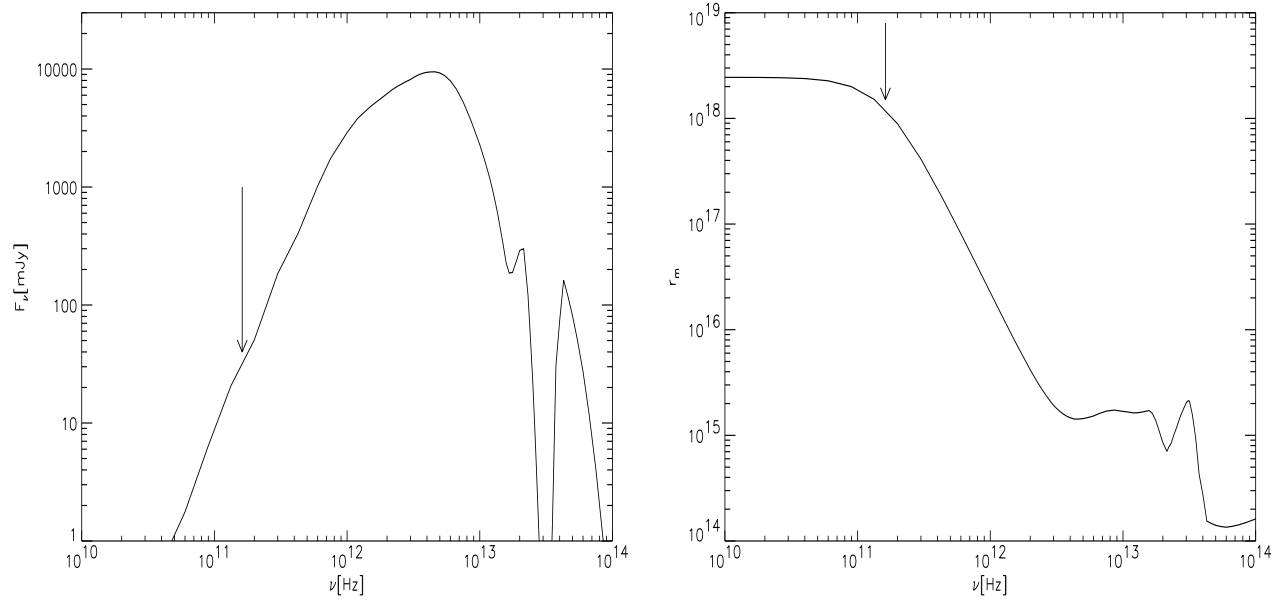


Fig. 11.— (a) SED for large \tilde{R}_c envelope (extended envelope) with break frequency marked, (b) Contribution function

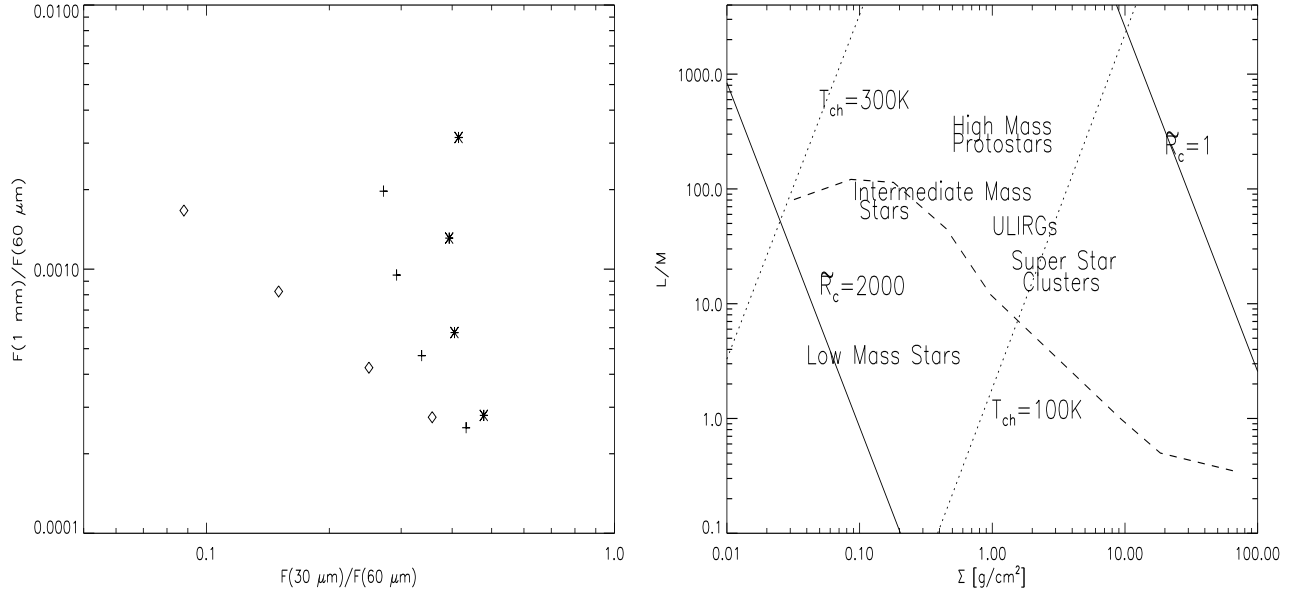


Fig. 12.— (a) $F(1\text{mm})/F(60\mu\text{m})$ vs $F(30\mu\text{m})/F(60\mu\text{m})$ for $k_\rho = 2$ (diamonds), $k_\rho = 3/2$ (crosses), $k_\rho = 1$ (asterisks); $k_\rho = 3/2$ curve corresponds to $T_{\text{ch}} = 210$ isotherm, (b) $L/M, \Sigma$ plot for $k_\rho = 3/2$, dashed line demarcates region below which density profiles can be inferred from far-IR SED